Supplementary Information for

Mercapto-functionalized scaffold improves perovskite buried interfaces for tandem photovoltaics

Jianan Wang[1,2]†, Shuaifeng Hu[3,4]†, He Zhu[1,2]†, Sanwan Liu[1]†, Zhongyong Zhang[5]†, Rui Chen[1], Junke Wang[3], Chenyang Shi[1], Jiaqi Zhang[1], Wentao Liu[1], Xia Lei[6], Bin Liu[5], Yongyan Pan[1], Fumeng Ren[1], Hasan Raza[1], Qisen Zhou[1], Sibo Li[7], Longbin Qiu[7], Guanhaojie Zheng[8], Xiaojun Qin[9], Zhiguo Zhao[9], Shuang Yang[10], Neng Li[5], Jingbai Li[11], Atsushi Wakamiya[4], Zonghao Liu[1,2]*, Henry J. Snaith[3]*, and Wei Chen[1,2]*

[1]Wuhan National Laboratory for Optoelectronics, Huazhong University of Science and Technology, Luoyu Road 1037, Wuhan, 430074, China.

[2]Optics Valley Laboratory, Hubei 430074, China.

[3]Clarendon Laboratory, Department of Physics, University of Oxford, Oxford OX1 3PU, UK.

[4]Institute for Chemical Research, Kyoto University, Gokasho, Uji, Kyoto 611-0011, Japan.

[5]State Key Laboratory of Silicate Materials for Architectures, Wuhan University of Technology, Wuhan 430070, China.

[6]Department of Materials Science and Engineering, Southern University of Science and Technology, Shenzhen, 518055 China.

[7]Shenzhen Key Laboratory of Intelligent Robotics and Flexible Manufacturing Systems, Department of Mechanical and Energy Engineering, SUSTech Energy Institute for Carbon Neutrality, Southern University of Science and Technology, Shenzhen, 518055, China.

[8]Shanghai Synchrotron Radiation Facility (SSRF), Zhangjiang Lab, Shanghai Advanced Research Institute, Chinese Academy of Sciences, Shanghai 201204, China.

[9]Huaneng Clean Energy Research Institute, Beijing 102209, China.

[10]School of Materials Science and Engineering, East China University of Science and

Technology, Meilong Road 130, 200237, Shanghai, China.

[11]Hoffmann Institute of Advanced Materials, Shenzhen Polytechnic University, Shenzhen, 518055, China.

†These authors contributed equally to this work.

Corresponding authors

liuzonghao@hust.edu.cn; henry.snaith@physics.ox.ac.uk; wnlochenwei@hust.edu.cn

The PDF file includes:

Supplementary Note 1: Comparison of storage stability of Al_2O_3, MSN and MSN-SH dispersions

For the dispersion of Al_2O_3, we chose the same specification as used in previous reports[1] (100 nm, 20 wt% isopropanol, Macklin). However, the diluted Al_2O_3 dispersion (20 mg mL^{-1} in isopropanol) ink is not stable during storage. As shown in **Supplementary Fig. 8**, the dispersed ink settled almost entirely after only 1 hour of storage, which will undoubtedly shorten the processing window of the devices and compromise the reproducibility of the device performance. This issue is frequently encountered with metal oxide particle dispersions due to the interparticle van der Waals interactions. The above issues of Al_2O_3 nanoparticles motivated us to seek well-dispersed dielectric nanoparticles to construct superstructure.

In terms of dielectric metal oxide nanoparticles, monodispersed MSN nanoparticles are also an excellent alternative due to their straightforward synthesis and customizable particle size. More importantly, the surface of MSN nanoparticles can be readily functionalized with various groups to enhance dispersion and confer special function[2]. We found that the use of (3-mercaptopropyl)trimethoxysilane (MPTS) instead of hydroxyl groups on the MSN surface can substantially improve the dispersibility and stability of MSN inks, with no sedimentation observed after 48 hours of storage. This improvement will largely broaden the process window and enhance the reproducibility of the superstructure layer.

Supplementary Note 2: Characterization of MSN and MSN-SH nanoparticles.

As shown in **Supplementary Fig. 9a**, after sulfhydryl functionalization, the average size of MSN particles was reduced from 110 nm to 100 nm and the particle size distribution was broadened. In terms of the porosity metrics, N_2 adsorption-desorption isotherm test was employed to investigate the porous structure evolution during the synthesis of MSN-SH. As indicated in **Supplementary Fig. 9b-d**, a typical type-IV hysteresis loop was observed, indicating the mesoporous nature of MSN and MSN-SH nanoparticles[3]. MSN-SH samples showed noticeable hysteresis loops only at relative pressure >0.8, similar to previous reports[4]. Notably, the total pore volume and average pore diameter of MSN-SH were 116.2 $m^2 g^{-1}$ and 3.4 nm, respectively, which were lower compared to 375.6 $m^2 g^{-1}$ and 6.1 nm for MSN. This phenomenon is common in the surface functionalization of mesoporous materials, which is caused by the presence of pendant groups on the surface of the functionalized material that partially prevent the adsorption of N_2 molecules[4,5].

We further observed the morphology of MSN and MSN-SH nanoparticles by transmission electron microscope (TEM). As shown in the **Supplementary Fig. 10a-b**, the sulfhydryl-modified particles remained uniformly spherical with a slight decrease in size, and the mesoporous pore structure was still present on the surface, but the pore-like structure was changed. We also tried to confirm the successful grafting of sulfhydryl groups on the surface of MSN particles by high-resolution EDS-TEM elemental mapping. However, unfortunately, we did not detect the corresponding strong S signals, which may be due to the amount of S is below the limit of detection. Instead, we conducted FTIR and Raman spectra tests with high detect sensitivity, which are widely used to verify the presence of characteristic groups on the surface of functionalized mesoporous materials to investigate this point as previously reports[4-8]. The Raman and FTIR spectra of MSN-SH samples showed characteristic peaks of sulfhydryl groups at 2569 cm^{-1} and 2563 cm^{-1}, respectively (**Supplementary Fig. 10c-d**). The successful grafting of sulfhydryl groups on the MSN surface was fully confirmed by combining the reductive validation experiments of MSN-SH in **Supplementary Figs. 20-21** and **Supplementary Note 5**.

Supplementary Note 3: Homogeneous and heterogeneous nucleation

Perovskite nucleation occurs either in a heterogeneous or homogeneous manner. According to classical theory, homogeneous nucleation is related to the total excess free energy. On the other hand, since heterogeneous nucleation occurs on foreign nuclei or surfaces, the extra surface or interface contact energy due to the wetting of foreign surfaces needs to be taken into consideration[9]. In the case of perovskite crystal formation, heterogeneous nucleation may dominate the growth mechanism since nucleation usually occurs on foreign surfaces or through nuclei. The relationship between the free energy for heterogeneous nucleation and that for homogeneous nucleation is given by the equation[10]:

$$\Delta G_{heterogeneous} = \Delta G_{homogeneous} \frac{(2 + \cos\theta)(1 - \cos\theta)^2}{4} \quad (1)$$

where θ is the contact angle between the crystalline deposit and the foreign solid surface, *i.e.* the wetting angle at the solid/liquid interface.

During the growth process of perovskite crystals, sufficient nucleation sites are required to achieve a compact film with complete coverage over the underlying substrate. As shown in **Supplementary Fig. 11**, the introduction of the MSN-SH layer results in better wettability (lower θ) of the perovskite precursor solution on the substrate, which can promote heterogeneous nucleation. On the other hand, due to the curvature of MSN-SH, the contact angle will be lower than that of the planar structure, which leads to a lower energy barrier for nucleation. Hence, the surface of MSN-SH with mesoporous structure provides enough heterogeneous nucleation sites to promote the rapid nucleation of Sn–Pb perovskite, which leads to the filling of voids at the buried interface of perovskite films.

Supplementary Note 4: The residual strain analysis

For GIXRD measurements, the peak position corresponding to the (210) plane of perovskite was chosen as the strain-free 2θ degree because of its versatility in providing more reliable information on structural symmetry. During the measurements, 2θ was fixed while the instrument tilt angles were varied to ensure the depth of X-ray penetration. The tilt angles (ψ) were fixed at 5, 15, 25, 35 and 45°. According to Bragg's law and generalized Hooke's law, the relationship of 2θ-$\sin^2\psi$ can be given by the following equation[11]:

$$\sigma = -\frac{E}{2(1+\upsilon)}\frac{\pi}{180}\cot\theta_0\frac{\partial(2\theta)}{\partial\sin^2\psi} \quad (2)$$

where E and υ respectively represent Young's modulus (10.2 GPa) and Poisson's ratio (0.33) of the perovskite film. θ_0 is half of the scattering angle $2\theta_0$ for strain-free perovskite ($2\theta_0$ = 31.6°). By fitting the 2θ as a function of $\sin^2\psi$, we can calculate the residual strain of perovskite film from equation (2), and the slope of the fitted line stands for the scale of the residual strain. The negative slope indicates the films bear the tensile strain, while the positive slope indicates the films bear the compressive strain[12].

Supplementary Note 5: Verification of MSN-SH reductivity

An additional consideration for the introduction of the MSN-SH layer was the desire to utilize the surface-modified sulfhydryl group to reduce undesirable oxidation reactions at the buried interface induced by acidic PEDOT:PSS under light or thermal stress. To verify the ability of MSN-SH to reduce I_2 and Sn(IV), we first added 4 mg of MSN and MSN-SH powder to 2 mL of I_2 aqueous solution (0.3 mM), respectively. After uniform shaking, it was visually observed that the I_2 aqueous solution containing MSN-SH powder rapidly changed from light brown to colorless. The darkening of the color of the I_2 aqueous solution containing MSN powder may be caused by the phenomenon of light scattering. Then the solution was centrifuged and the supernatant was used for UV-Vis measurements. As shown in **Supplementary Fig. 20**, MSN has a capturing effect on I_2, while MSN-SH reduces I_2. We carried out the same operation and observed that MSN-SH can inhibit the oxidation of Sn(II) in the perovskite precursor solution, which is of great significance in enhancing the stability of the buried interface. To gain further insight into the mechanism of the inhibition of Sn(II) oxidation by MSH-SH, we conducted cyclic voltammetry (CV) measurements to evaluate the redox potentials associated with the sulfhydryl group in pure SnI_2 solution[13], using butanethiol as a sulfhydryl groups provider. As shown in **Supplementary Fig. 21c**, obvious oxidation and reduction peaks are observed in the CV curves, and the redox potential ($E_{1/2}$) is determined by averaging the cathode potential ($E_{p,c}$) and anode potential ($E_{p,a}$). From the $E_{p,a}$ and $E_{p,c}$ in the control cyclic voltammetry curve, $E_{1/2}$ was calculated to be −0.545 V. The $E_{1/2}$ of the sample containing sulfhydryl species rises to −0.370 V compare to the control sample. This observation suggests that the SnI_2-SH complex is less susceptible to oxidation, which is consistent with the experimental phenomenon.

Supplementary Note 6: Open-circuit voltage (V_{OC}) and fill factor (FF) and loss analysis

Following the assumption of the radiative limit, the total V_{OC} loss can be described by the equation listed below:

$$q\Delta V = E_g - qV_{OC} = (E_g - qV_{OC}^{SQ}) + (qV_{OC}^{SQ} - qV_{OC}^{rad}) + (qV_{OC}^{rad} - qV_{OC})$$

$$= \Delta E_1 + \Delta E_2 + \Delta E_3 = q(\Delta V_1 + \Delta V_2 + \Delta V_3) \quad (3)$$

Where q is the elementary charge, E_g is the bandgap of perovskite. V_{OC}^{SQ} is the maximum V_{OC} under the S-Q limit. V_{OC}^{rad} is the V_{OC} without non-radiative recombination occurring in devices, ΔE_1 is the V_{OC} loss due to the non-ideal EQE above the bandgap, ΔE_2 is the V_{OC} loss due to the sub-bandgap radiative recombination. ΔE_3 is the V_{OC} loss associated with the non-radiative recombination is given by:

$$\Delta E_3 = q\Delta V_3 = -k_B T \ln(\mathrm{EQE_{EL}}) \quad (4)$$

The external quantum efficiency of the electroluminescence (EQE_{EL}) of the device was obtained when the injection current density was close to the J_{SC} under solar illumination.

The FF losses in solar cells are determined by two main components: non-radiative recombination loss and charge transport loss[1]. The maximum FF (FF_{max}) can be empirically calculated according to the following equation:

$$FF_{max} = \frac{v_{OC} - \ln(v_{OC} + 0.72)}{v_{OC} + 1} \quad (5)$$

where $v_{OC} = \frac{V_{OC}}{nk_BT/q}$, n is ideality factor, k_B is Boltzmann constant, T is the temperature (300 K), q is the elementary charge. n is obtained from the V_{OC} as a function of light intensity on a logarithmic scale, which is shown in **Supplementary Fig. 27**.

Supplementary Note 7: The quasi-Fermi level spitting (QFLS) analysis

To quantify the open-circuit voltage potential for neat perovskite and every individual stack, we calculated the Quasi–Fermi level splitting (QFLS) values from PLQY results by using the following equation[14]:

$$QFLS = QFLS_{\text{rad}} + k_B T \cdot \ln(\text{PLQY}) = k_B T \cdot \ln(\text{PLQY} \frac{J_G}{J_{0,rad}}) \quad (3)$$

where k_B is Boltzmann's constant, and T is the temperature (300 K). J_G is the photogenerated current density under 1 sun, it is approximated with the short-circuit current density of devices. $J_{0,\text{rad}}$ is the radiative recombination current in the dark, it is obtained by integrating the overlap of the external quantum efficiency of the device (EQE_{PV}) with the black-body radiative spectrum (ϕ_{BB}) at 300 K over the energy, based on the following equations:

$$J_{0,rad} = q \int_0^\infty \text{EQE}_{\text{PV}}(E) \phi_{BB}(E)\, dE \quad (4)$$

$$\phi_{BB}(E) = \frac{2\pi}{h^3 c^2} \frac{E^2}{exp\left(\frac{E}{k_B T}\right) - 1} \quad (5)$$

where q is the elementary charge, E is the photon energy, h is the Planck constant, and c is the light speed in vacuum. As shown in **Supplementary Fig. 31**, the value of $J_{0,\text{rad}}$ is 1.2×10^{-15} mA cm^{-2} for all devices independent of the bottom insert layer.

Supplementary Note 8: The role of the alkyl sulfhydryl group in enhancing device performance

As illustrated in **Supplementary Fig. 7**, MSN-SH particles were derived from MPTS functionalized MSN. To systematically evaluate the influence of sulfhydryl groups alone (without nanoparticles), we post-treated the PEDOT:PSS substrates with MPTS solutions at varying concentrations (2, 4, and 8 mg mL^{-1} dissolved in isopropanol). Similar to the results in **Supplementary Fig. 1**, distinct "white" spots are still observed from the glass side of the perovskite films on the PEDOT: PSS/MPTS-coated ITO substrate. The cross-sectional SEM images of the corresponding films further confirm that MPTS post-treatment alone fails to eliminate the nanovoids at the buried interface (**Supplementary Fig. 4-5**). In contrast, MSN or MSN-SH post-treatment effectively eliminates these nanovoids, demonstrating that the mesoporous structure of the nanoparticles is essential for achieving improved interfacial contact at the bottom interface.

Notably, we found that the MSN-SH layer plays a more positive impact on enhancing the crystallinity of the perovskite near the buried interface and suppressing the non-radiative recombination when compared with the MSN-based sample (**Fig. 1d-f**, **Supplementary Fig. 14**). Additionally, we observed that both MSN and MSN-SH layers had the ability to release residual tensile stress in the Sn–Pb perovskite films (**Fig. 1h**, **Supplementary Fig. 15**). These results suggested that the alkyl sulfhydryl group on the surface of MSN for MSN-SH superstructure can regulate the perovskite crystallization process and passivate defects through interactions with the perovskite material.

The mechanical strength test results showed that the critical tensile strength at the perovskite/PEDOT:PSS interface was approximately 0.26 MPa , with a fracture energy of 25 kJ m^{-3} at 0.17% strain. The introduction of the MSN layer helped to eliminate the nanovoids, which in turn increased the critical tensile strength and fracture energy to 0.39 MPa and 47 kJ m^{-3} at 0.26% strain at the perovskite/MSN/PEDOT:PSS interface. Furthermore, the MSN-SH nanoparticles, with abundant -SH groups, formed strong

bonds with perovskite, thereby further increasing the critical tensile strength and fracture energy to 0.67 MPa and 83 kJ m^{-3} at 0.29% strain (**Fig. 1g**). Collectively, these results confirm that the MSN-SH layer is capable of mechanically reinforcing buried interface through the elimination of nanovoids and the promotion of cohesive adhesion[15].

As elaborated in the manuscript, we expect that the sulfhydryl group modified on the silica matrix is able to reduce the concentrations of V_{Sn} and V_I at the buried interface as well as increase the iodide migration barrier through strong interactions with the metal cations (i.e., Sn(II) and Pb(II)) and thus hinder the decomposition of perovskite at the buried interface under light or/and thermal stress. The DFT results revealed that the introduction of the sulfhydryl group leads to a significant enhancement of the V_I formation energy and enhanced ion migration barrier (**Fig. 2a and Supplementary Fig. 18**). Temperature-dependent conductivity tests confirmed that the sulfhydryl group inhibited ion migration in the perovskite films. The MSN-SH sample showed the highest ion migration barrier of 0.58 eV compared to the control (0.29 eV) and MSN (0.45 eV) samples (**Fig. 2b-d**), which demonstrated the role of the sulfhydryl group in enhancing the stability of the buried interface. The MSN-SH-based devices show improved efficiency and stability due to the reduction of non-radiative recombination and the increased chemical and mechanical stability at the interface (refer to **Fig. 3, Supplementary Fig. 32, and Supplementary Table 4**). This demonstrates the significant role of the sulfhydryl group in enhancing device performance.

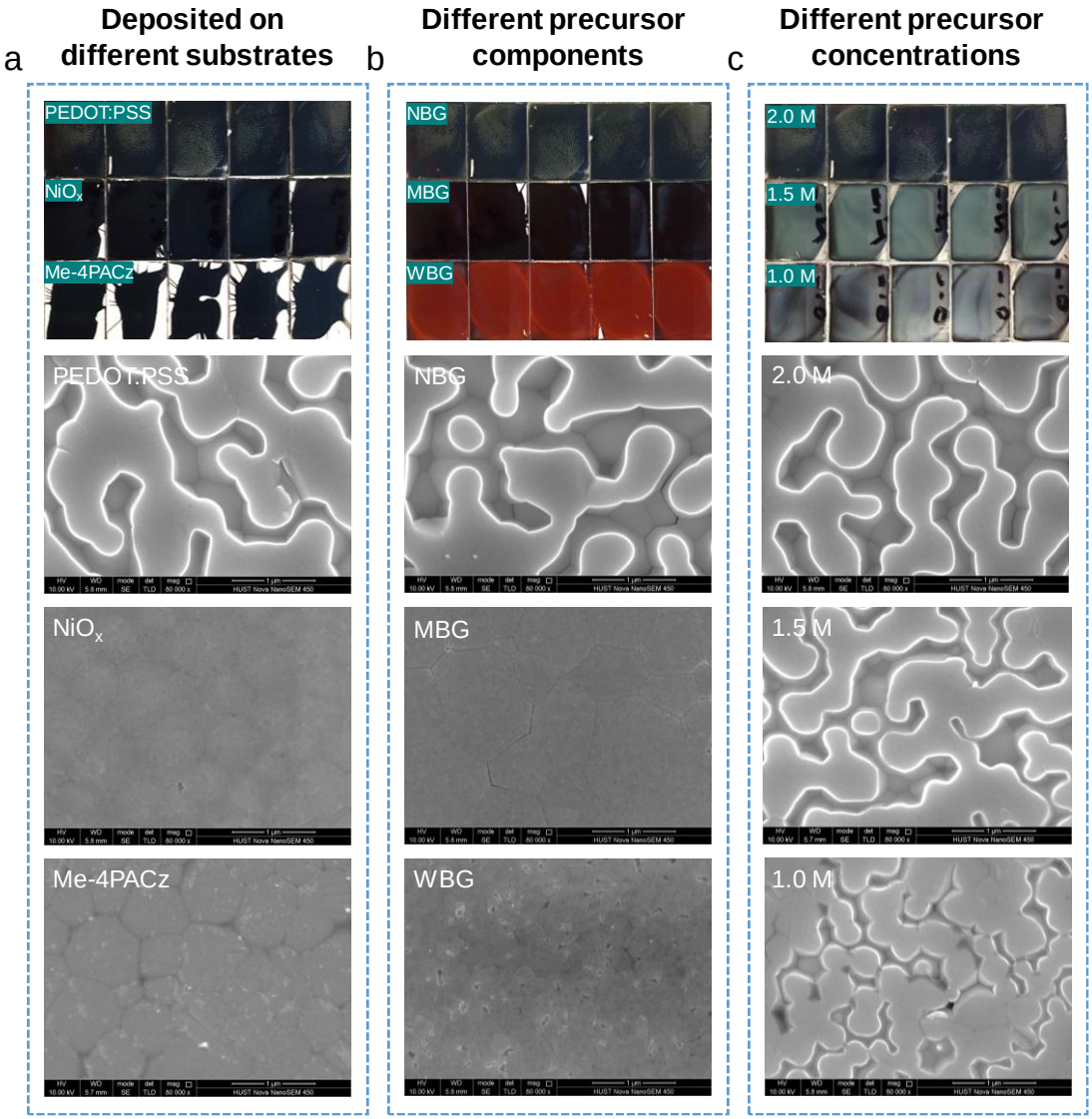

Supplementary Fig. 1. (**a**) Photographs (glass side) and SEM images of the bottom surface of narrow-bandgap Sn–Pb perovskite films deposited on PEDOT:PSS-, NiO_x-, and Me-4PACz-based substrates, respectively. (**b**) Photographs (glass side) and SEM images of the bottom surface of narrow-bandgap (NBG, $Cs_{0.1}FA_{0.6}MA_{0.3}Pb_{0.5}Sn_{0.5}I_3$), middle-bandgap (MBG, $FA_{0.98}Cs_{0.02}PbI_3$) and wide-bandgap (WBG, $FA_{0.8}Cs_{0.2}Pb(I_{0.6}Br_{0.4})_3$) perovskite films deposited on PEDOT: PSS-coated substrates. (**c**) Photographs (glass side) and SEM images of the bottom surface of NBG perovskite films deposited on PEDOT:PSS-coated substrates at 1.0, 1.5 and 2.0 M perovskite precursor concentrations.

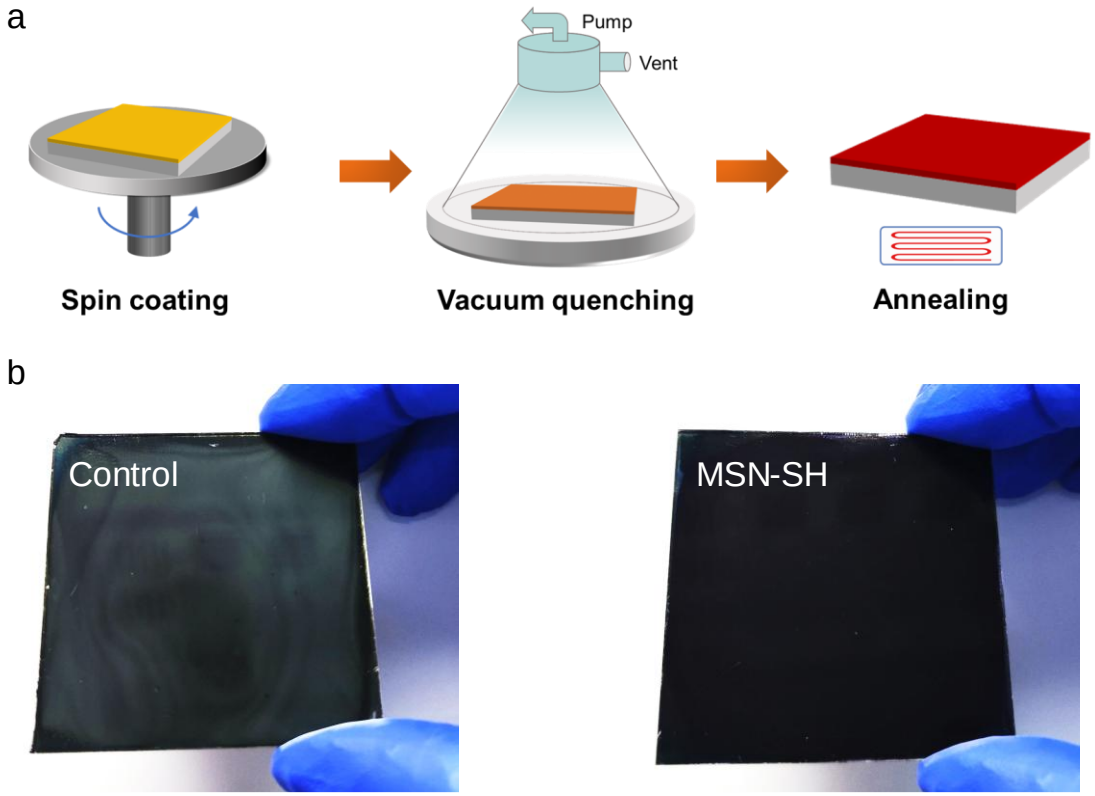

Supplementary Fig. 2. (**a**) Schematic diagram of large-area Sn–Pb perovskite films prepared by vacuum-assisted crystallization method. (**b**) Photographs (glass side) of Sn–Pb perovskite films deposited on PEDOT:PSS- and PEDOT:PSS/MSN-SH-coated substrates, respectively.

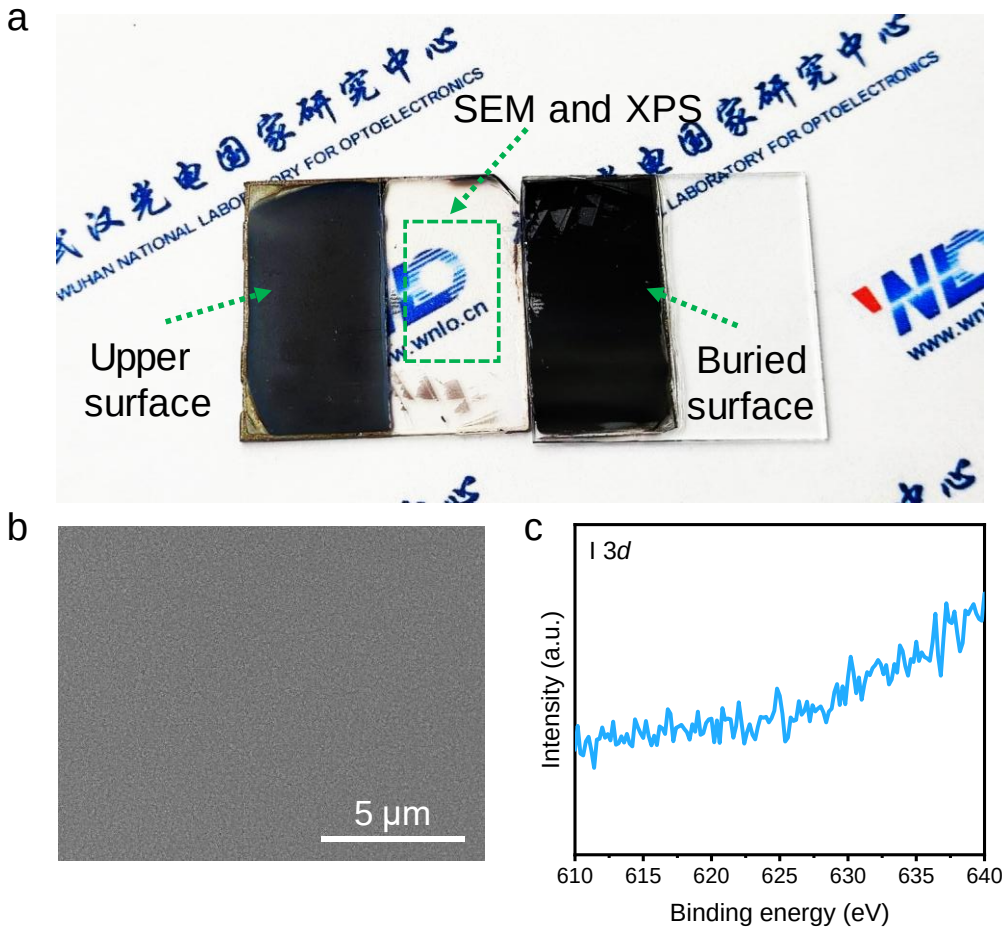

Supplementary Fig. 3. (**a**) Complete separation of the perovskite film from the substrate, exposing the partially buried interface of the perovskite film and corresponding substrate region. (**b**) SEM image of the substrate region, no perovskite grain residues observed. (**c**) XPS result of I 3*d* in substrate region, no significant signal was observed.

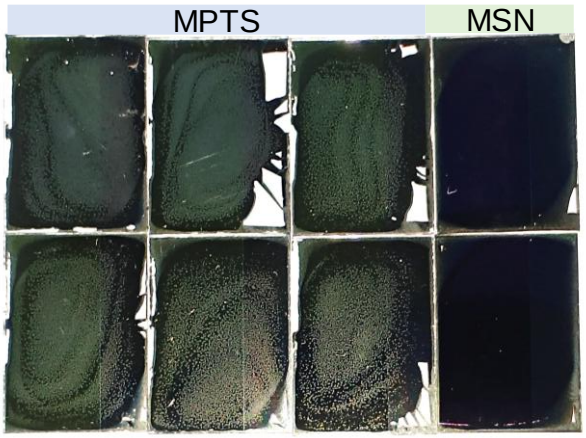

Supplementary Fig. 4. Photographs (glass side) of the bottom surface of Sn–Pb perovskite films deposited on PEDOT:PSS/MPTS- and PEDOT:PSS/MSN-coated substrates, respectively. The concentrations of MPTS solutions for PEDOT:PSS substrate post-treatment were set at 2, 4, and 8 mg mL^{-1} (dissolved in isopropanol).

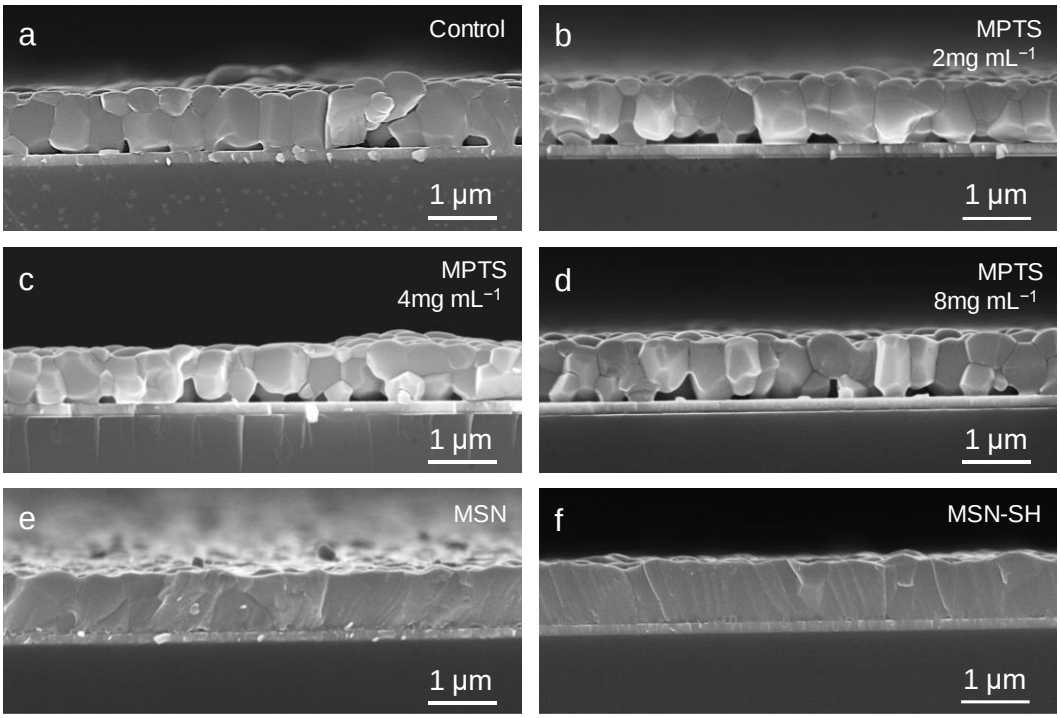

Supplementary Fig. 5. Cross-section SEM images of perovskite films deposited on (**a**) PEDOT:PSS-, (**b-d**) PEDOT:PSS/MPTS-, (**e**) PEDOT:PSS/MSN-, and (**f**) PEDOT:PSS/MSN-SH-coated ITO substrates, respectively.

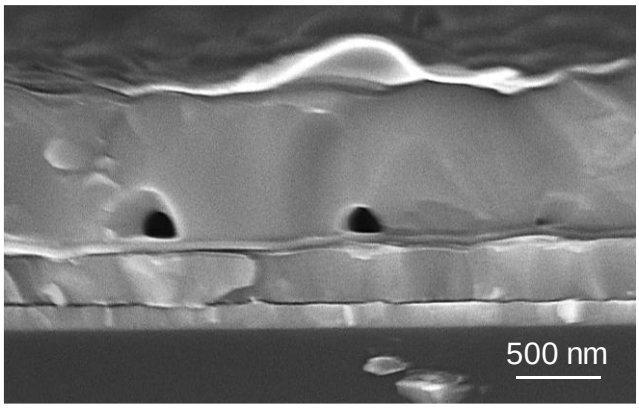

Supplementary Fig. 6. Cross-section SEM images of all-perovskite tandem solar cell without the MSN-SH layer.

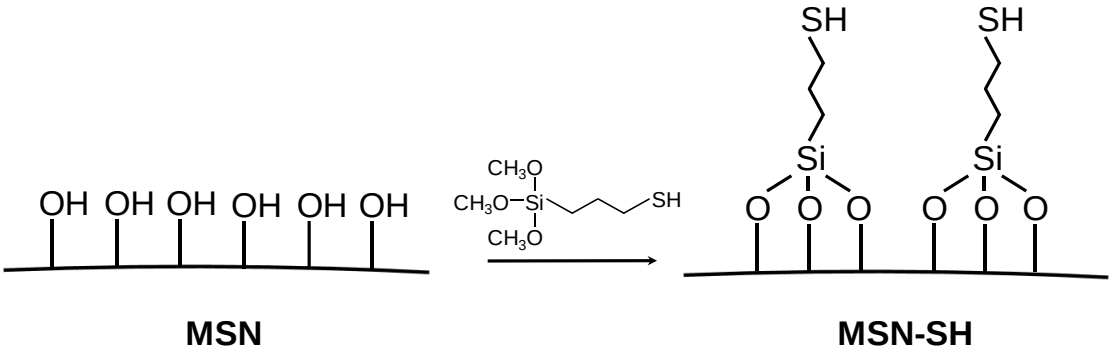

Supplementary Fig. 7. Schematic representation of mercapto-functionalized mesoporous silica nanoparticles.

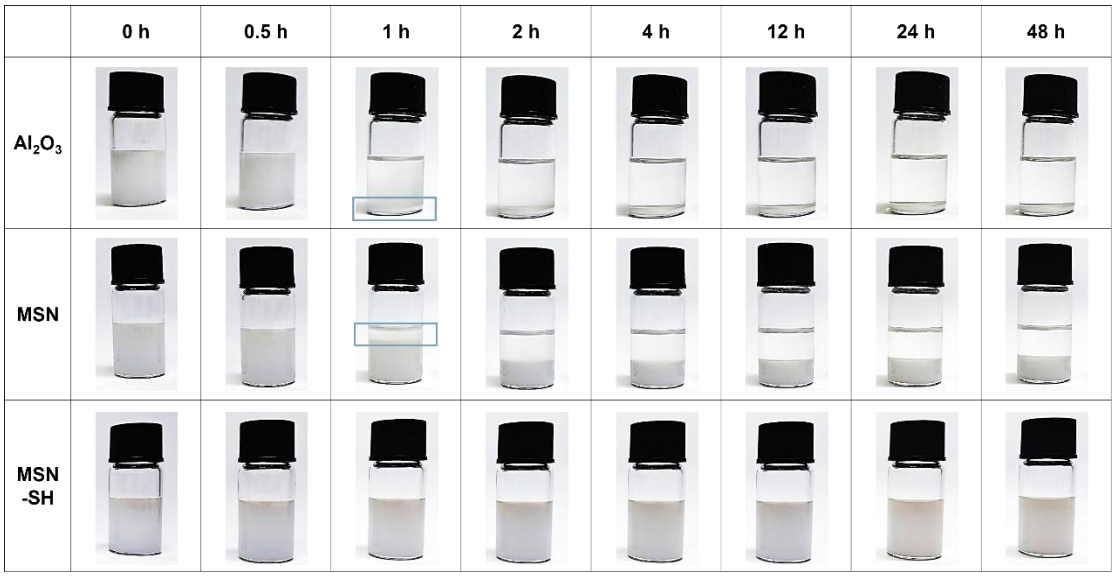

Supplementary Fig. 8. Storage stability of Al_2O_3, MSN, and MSN-SH dispersions with particle sizes of 100 nm and concentrations of 20 mg mL^{-1} in isopropanol.

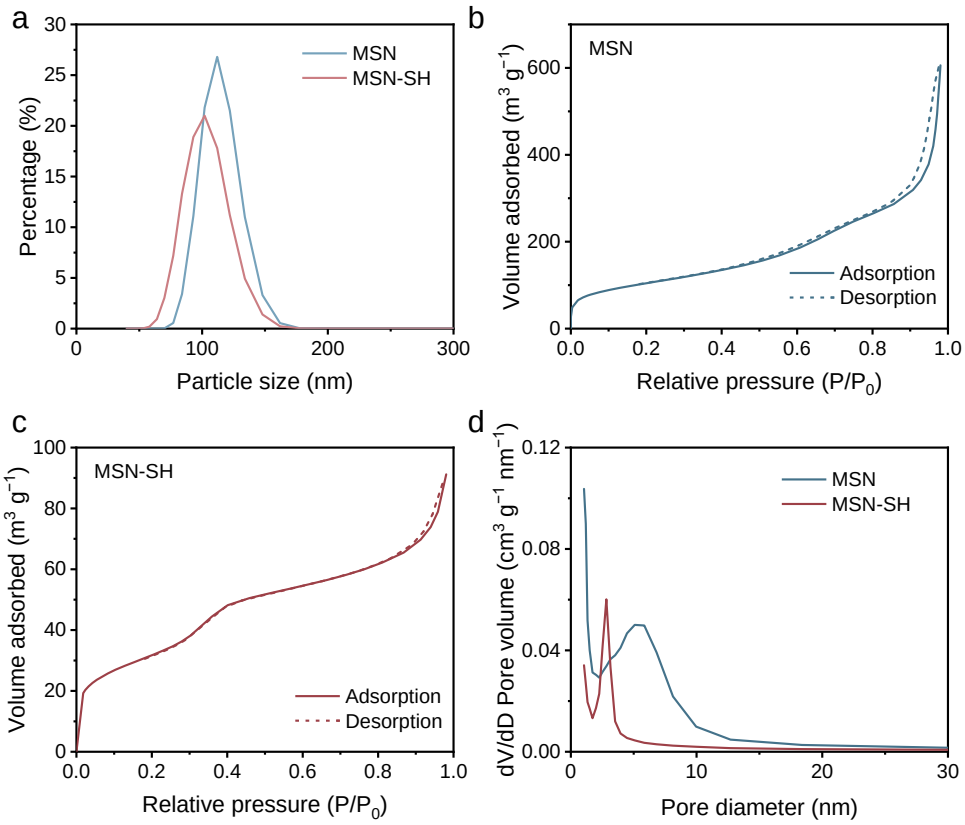

Supplementary Fig. 9. (**a**) Particle size distribution of MSN and MSN-SH nanoparticles. N_2 adsorption/desorption isotherms of (**b**) MSN and (**c**) MSN-SH nanoparticles. (**d**) Pore diameter distribution of MSN and MSN-SH nanoparticles.

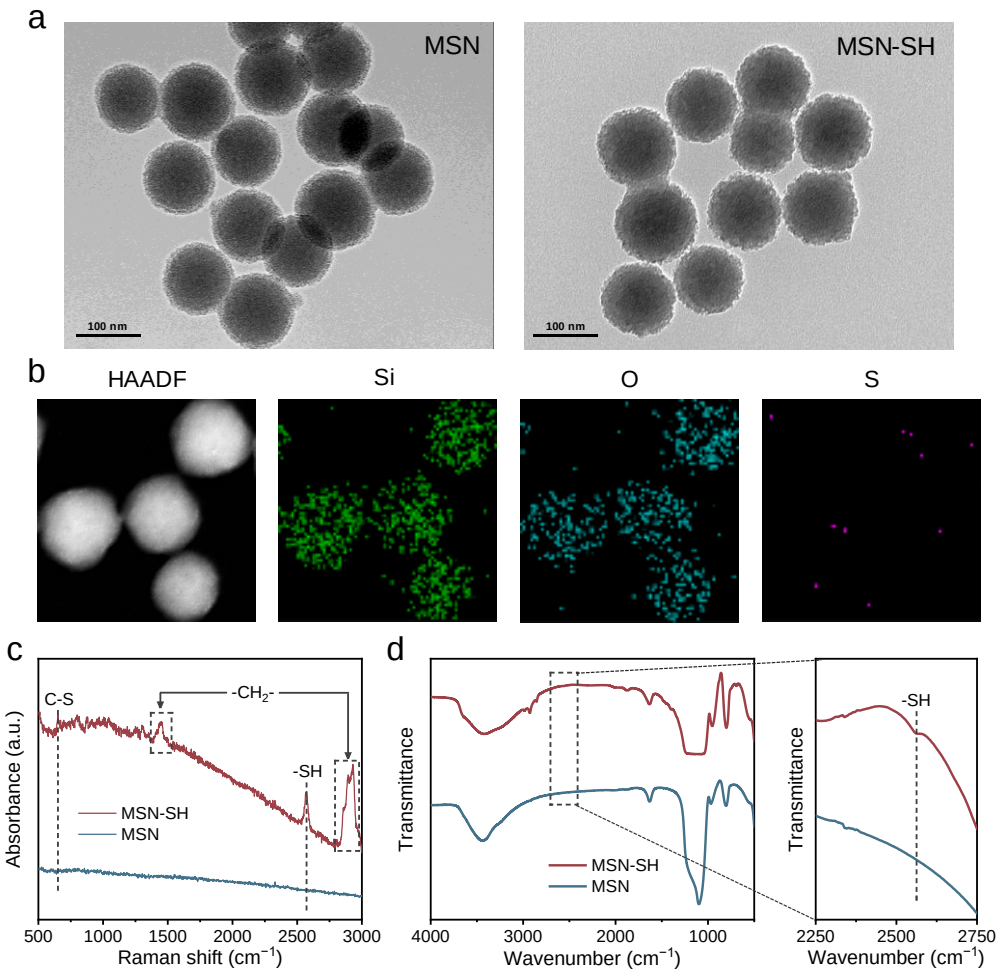

Supplementary Fig. 10. (**a**) TEM images of MSN and MSN-SH nanoparticles. (**b**) EDS mapping of the MSN-SH nanoparticles. (**c**) Raman and (**d**) FTIR spectra of MSN and MSN-SH nanoparticles.

Supplementary Fig. 11. Contact angles of the NBG perovskite precursor solution on (**a**) PEDOT:PSS-, (**b**) PEDOT:PSS/MSN-, and (**c**) PEDOT:PSS/MSN-SH-coated substrates.

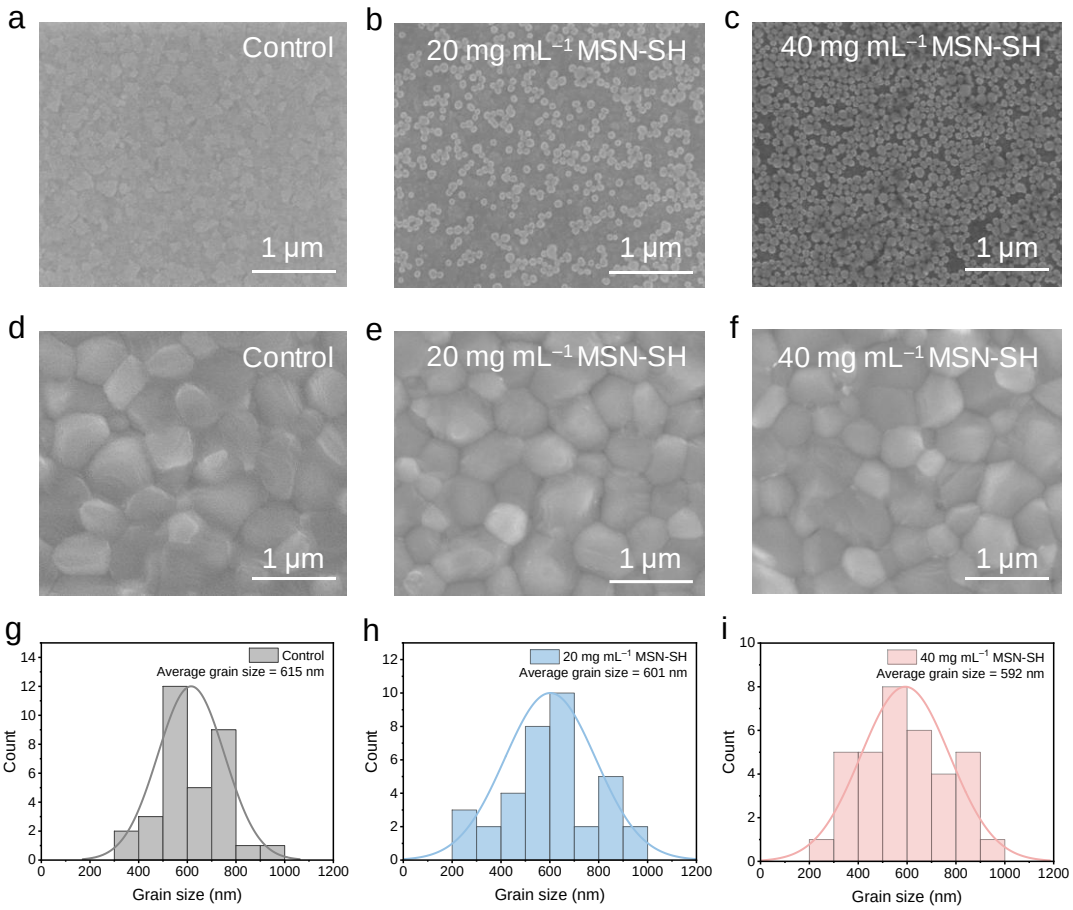

Supplementary Fig. 12. SEM images of MSN-SH deposited on ITO/PEDOT:PSS-coated substrates with (**a**) 0, (**b**) 20, and (**c**) 40 mg mL^{-1} dispersion concentrations. SEM images of Sn–Pb perovskite films deposited on the PEDOT:PSS/MSN-SH-coated substrates with (**d**) 0, (**e**) 20, and (**f**) 40 mg mL^{-1} dispersion concentrations of MSN-SH. Grain size distribution of the corresponding perovskite films deposited on the PEDOT:PSS/MSN-SH-coated substrates with (**g**) 0, (**h**) 20, and (**i**) 40 mg mL^{-1} dispersion concentrations of MSN-SH.

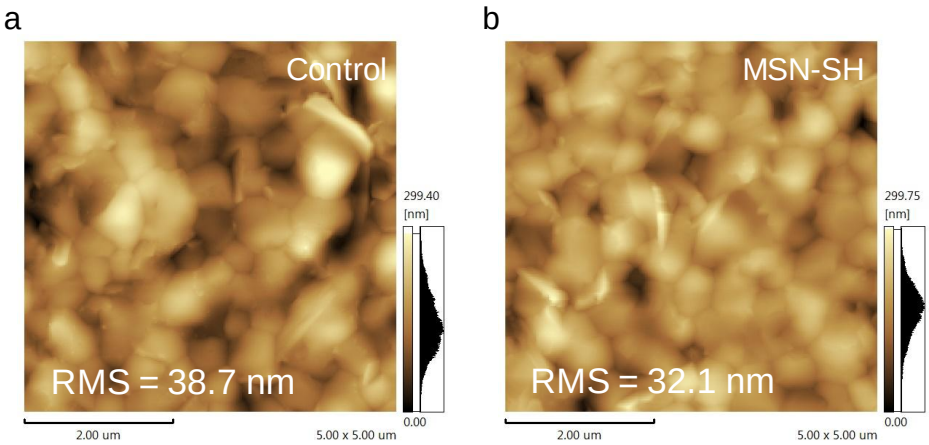

Supplementary Fig. 13. AFM images of perovskite films deposited on (**a**) PEDOT:PSS and (**b**) PEDOT:PSS/MSN-SH (20 mg mL^{-1}) substrates.

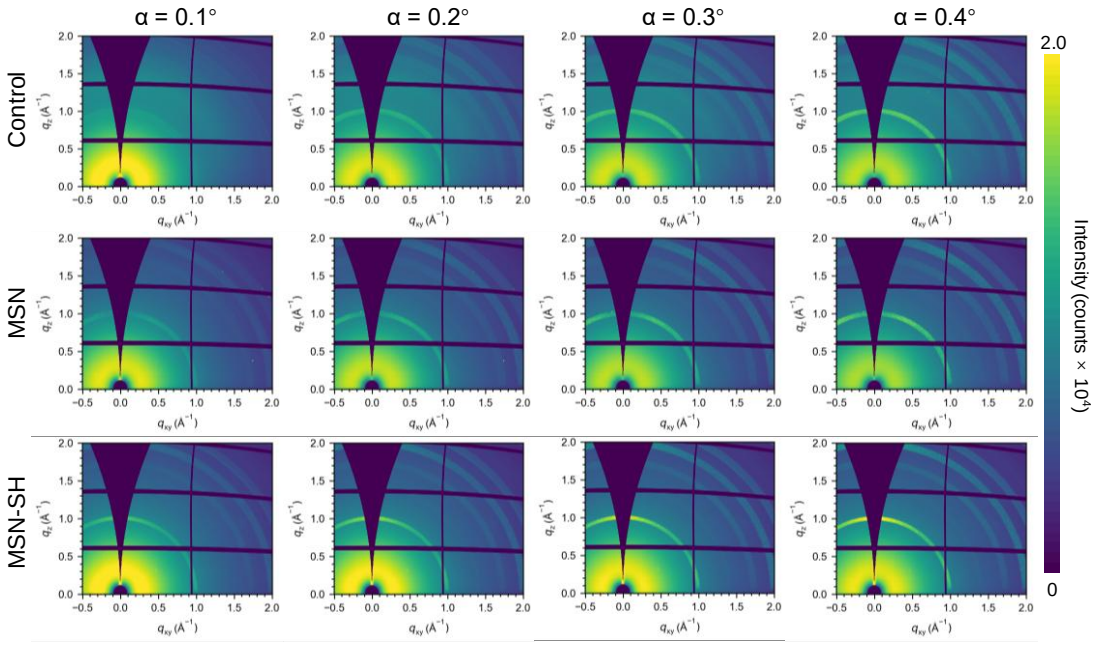

Supplementary Fig. 14. GIWAXS patterns that performed on the exposed buried interface of control, MSN, and MSN-SH perovskite film with different incidence angles.

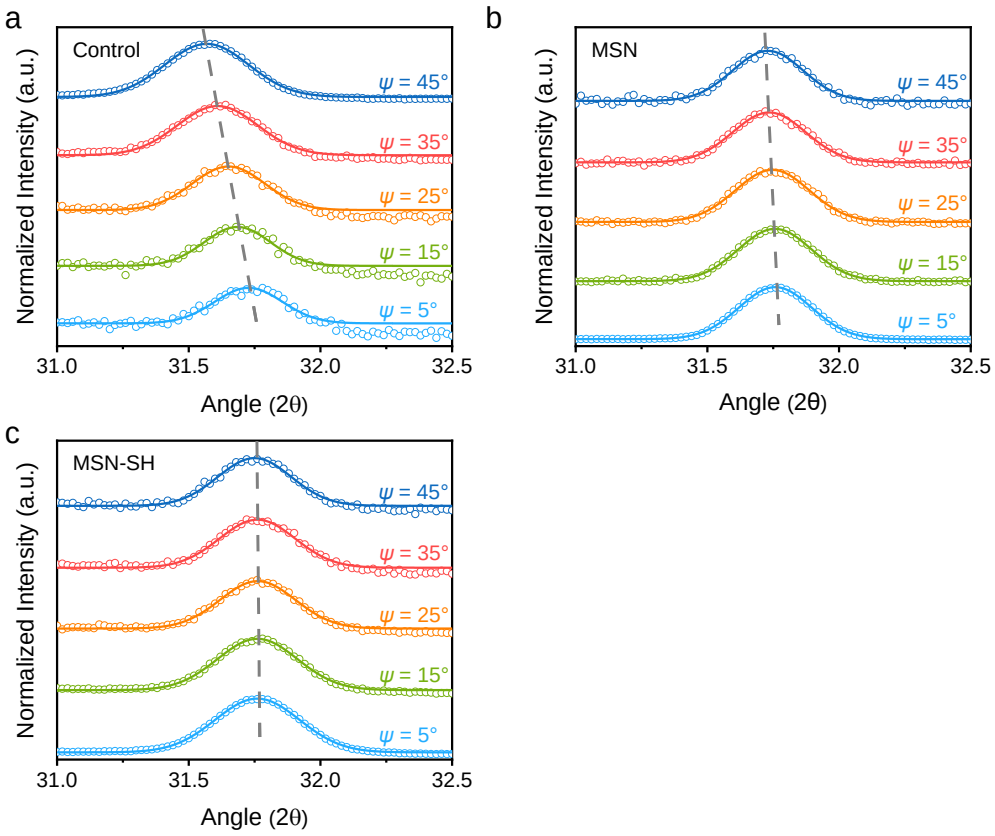

Supplementary Fig. 15. GIXRD patterns were obtained from the exposed buried interface of the (**a**) control, (**b**) MSN, and (**c**) MSN-SH perovskite film at different tilt angles ranging from 5° to 45°, using an incidence angle of 0.3°. The residual strain was evaluated by linearly fitting the 2θ-$\sin^2\psi$ plot for the control, MSN, and MSN-SH perovskite films, resulting in a calculated tensile stress of 72.2, 14.7, and 4.6 MPa, respectively.

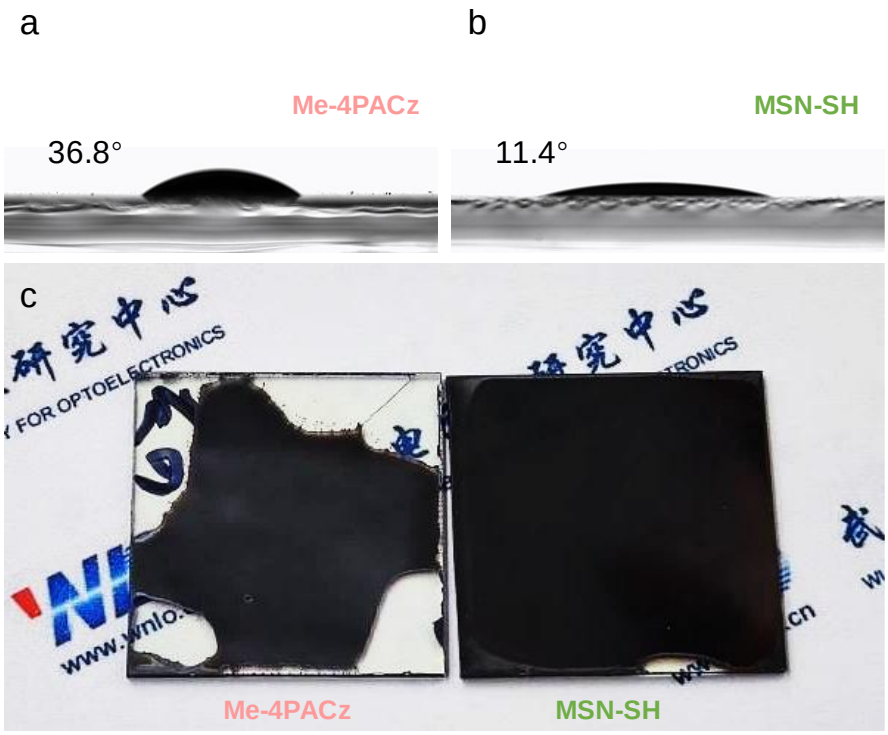

Supplementary Fig. 16. Contact angles of the WBG perovskite precursor solution on (**a**) Me-4PACz and (**b**) Me-4PACz/MSN-SH substrates. (**c**) Photographs of WBG perovskite film coverage on Me-4PACz and Me-4PACz/MSN-SH substrates.

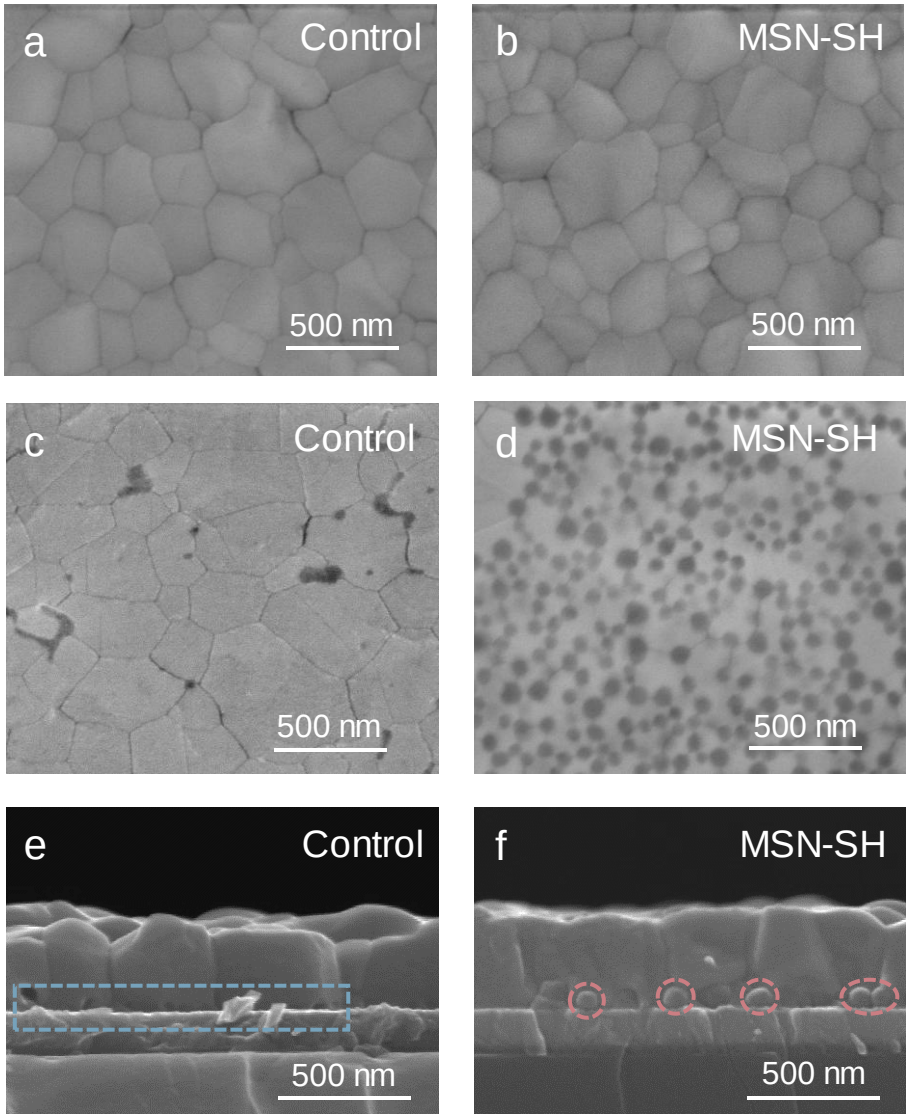

Supplementary Fig. 17. SEM images of WBG perovskite film deposited on (**a**) Me-4PACz and (**b**) Me-4PACz/MSN-SH substrates. SEM images of the buried interface of perovskite films deposited on (**c**) Me-4PACz and (**d**) Me-4PACz/MSN-SH substrates. Cross-section SEM images of perovskite films deposited on (**e**) Me-4PACz and (**f**) Me-4PACz/MSN-SH substrates. The beads at the buried interface (pink rounded box in **Supplementary Fig. 17f**) are the MSN-SH particles illustrated in **Supplementary Fig. 12b**.

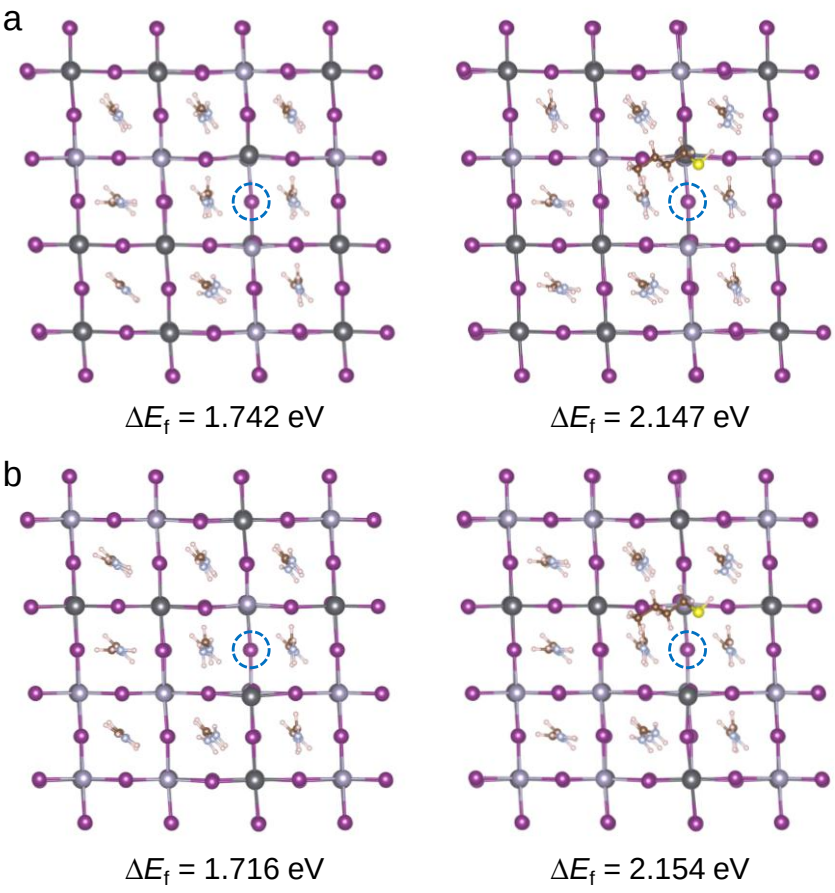

Supplementary Fig. 18. Lattice model employed for the theoretical computation, in which butanethiol adsorbed on Sn atom in the exposed (100) crystal plane was employed (top view). V_I defect (blue rounded box) was created on the exposed (100) plane of the perovskite. The formation energy of V_I was calculated for scenarios where butanethiol interacts with (**a**) Pb(II) and (**b**) Sn(II) within the perovskite lattice.

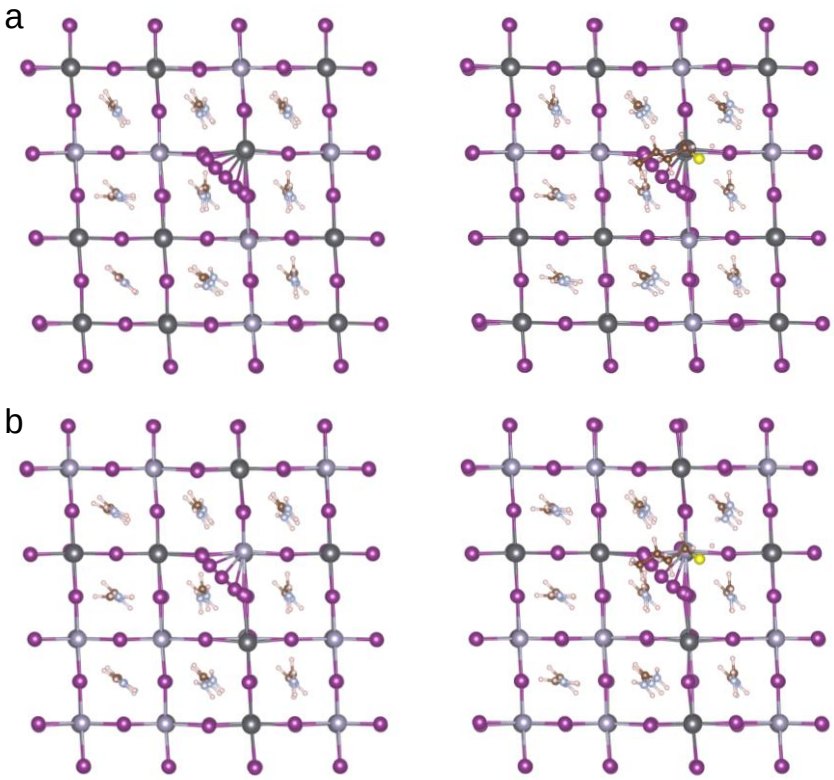

Supplementary Fig. 19. Top-view atomic configurations of iodine migration along the migration path when the sulfhydryl group is adsorbed on (**a**) Pb and (**b**) Sn atom of the perovskite lattice.

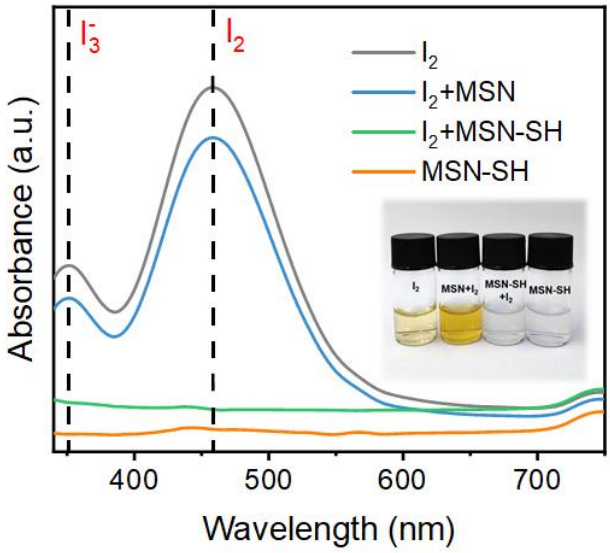

Supplementary Fig. 20. UV-vis absorption spectra of I_2 aqueous solution without and with MSN or MSN-SH treatment, and MSN-SH dispersed solution. Inset: photographs of I_2 aqueous solution without and with MSN or MSN-SH treatments, and MSN-SH dispersed solution.

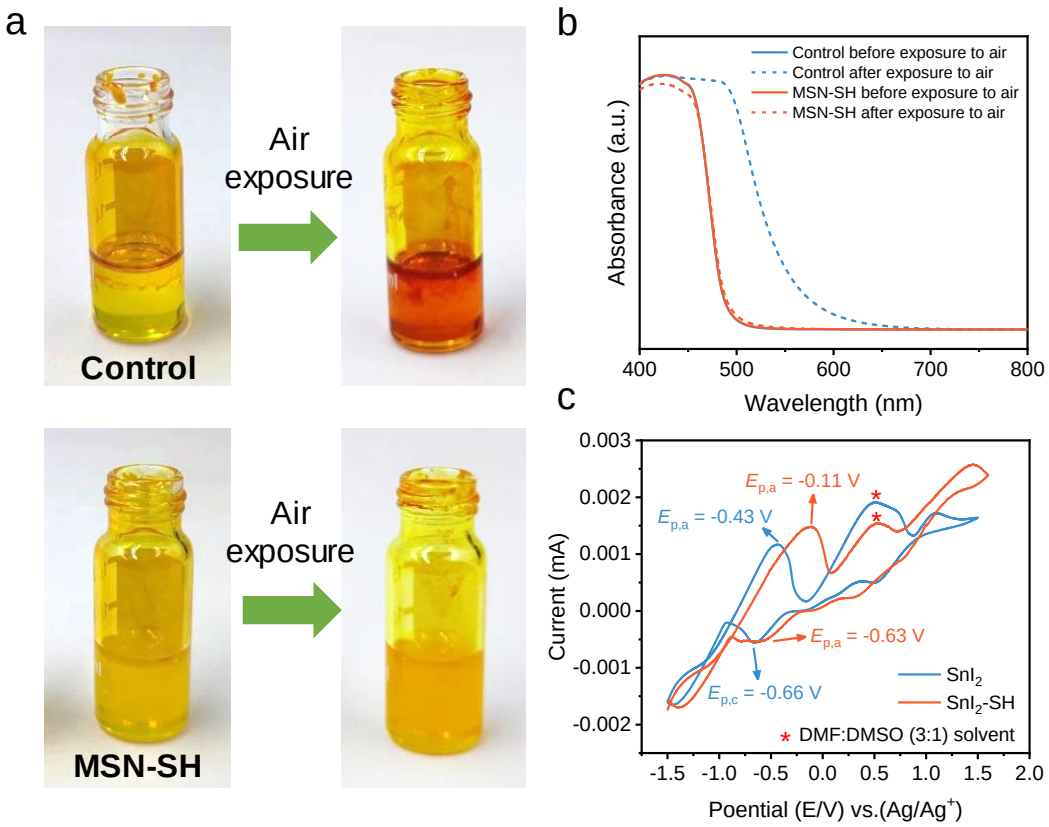

Supplementary Fig. 21. (**a**) Photographs and (**b**) UV-vis absorption spectra of control and MSN-SH mixed Sn–Pb perovskite precursor solutions before and after exposure to ambient air for 20 minutes. (**c**) CV curves of the SnI_2 solution without and with butanethiol containing sulfhydryl group.

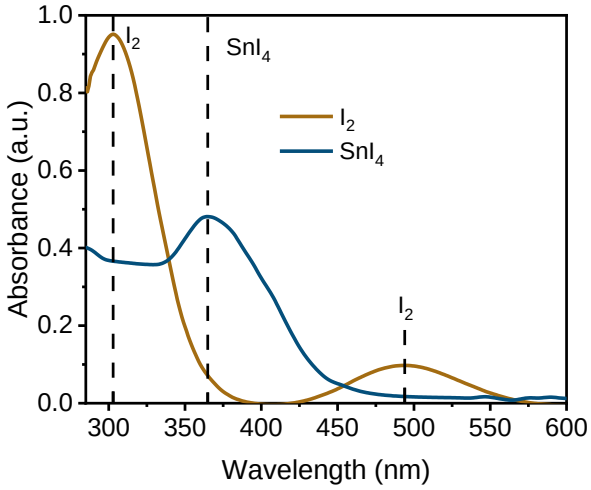

Supplementary Fig. 22. Absorbance spectra of I_2 and SnI_4 dissolved in toluene. As shown in **Fig. 2e**, no notable I_2 and SnI_4 absorption peaks were detected in the toluene solution with perovskite films deposited on ITO or PEDOT:PSS/MSN-SH substrates. In addition, the MSN layer slows down the I^- oxidation in the film likely by eliminating the voids at the buried interface, and the intensity of the I_2 and SnI_4 absorption peaks is lower than that of PEDOT:PSS-coated substrates.

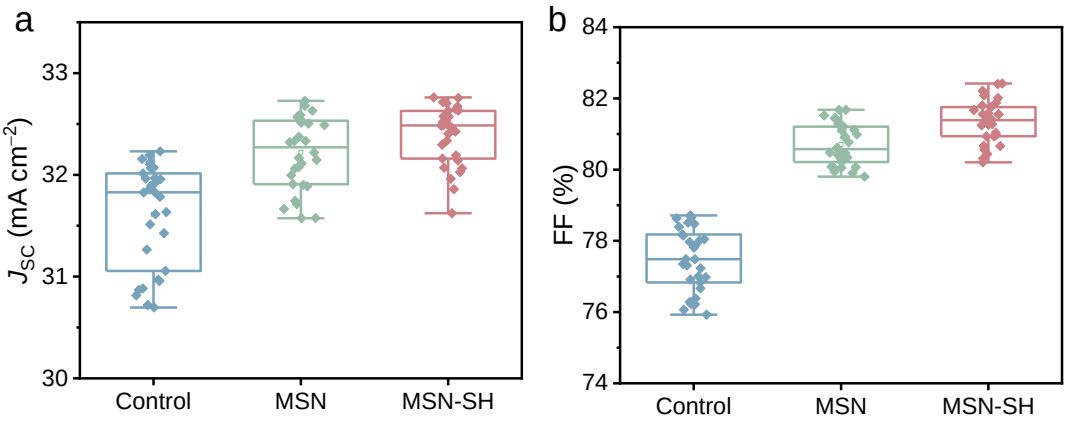

Supplementary Fig. 23. Statistical distribution of (**a**) J_{SC} and (**b**) FF for control, MSN, and MSN-SH Sn–Pb PSCs based on 30 devices.

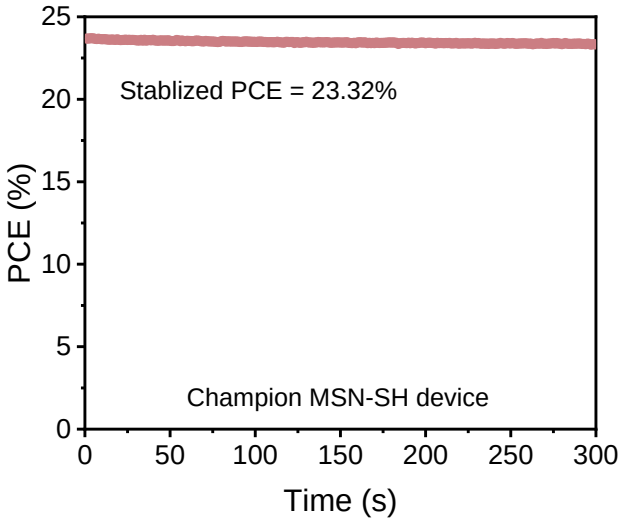

Supplementary Fig. 24. Stabilized power output of the champion MSN-SH Sn–Pb PSC measured by fixing the voltage at 0.74 V under AM1.5G illumination.

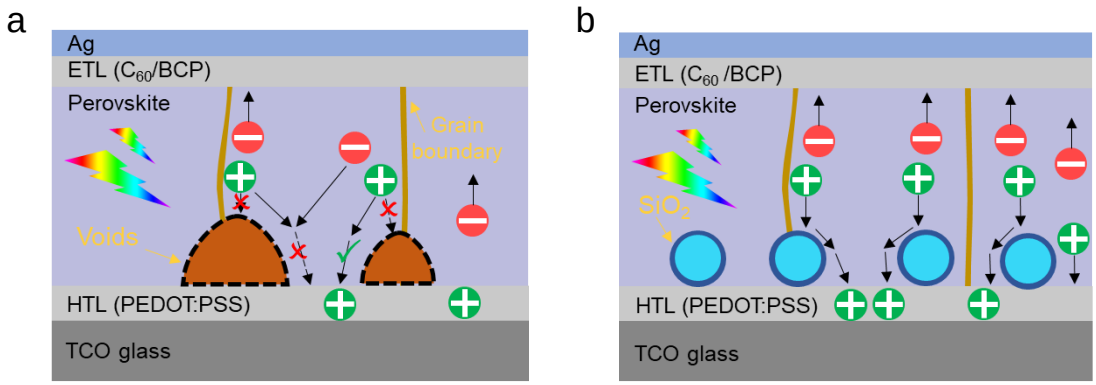

Supplementary Fig. 25. Schematic of the charge extraction process in Sn–Pb PSCs with (**a**) void-containing and (**b**) void-free buried interfaces.

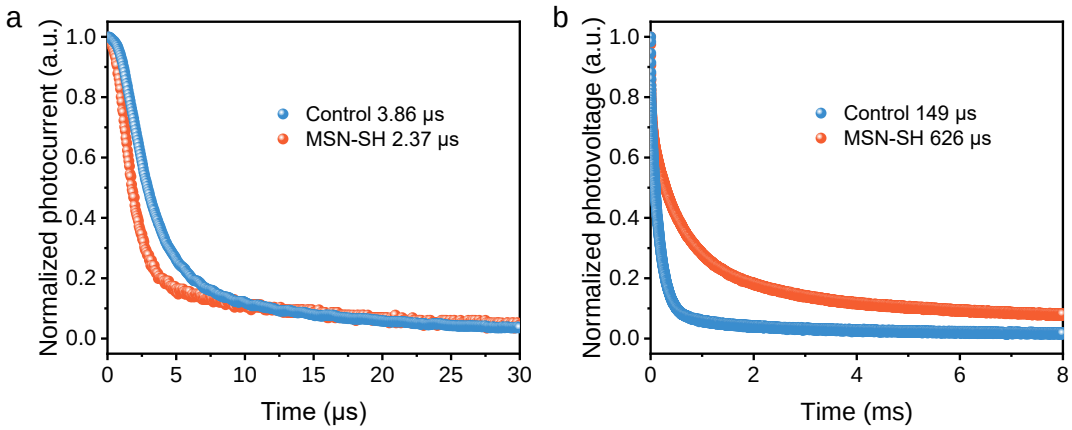

Supplementary Fig. 26. (**a**) Transient photocurrent (TPC) and (**b**) Transient photovoltage (TPV) plots of control and MSN-SH Sn–Pb PSCs.

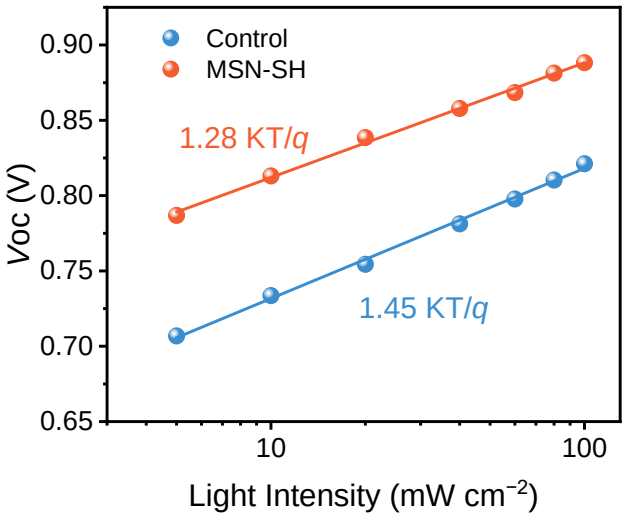

Supplementary Fig. 27. Light intensity dependence of V_{OC} for the control and MSN-SH Sn–Pb PSCs.

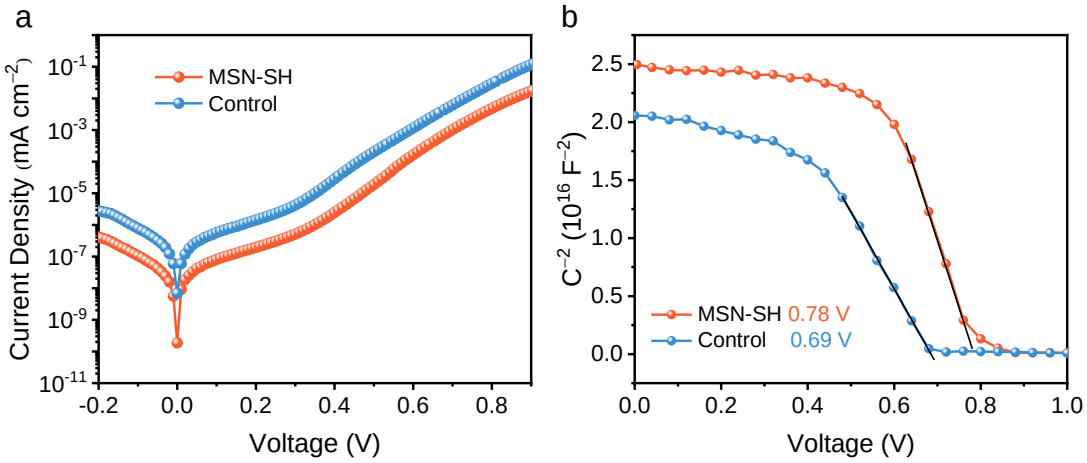

Supplementary Fig. 28. (**a**) Dark *J*–*V* curves and (**b**) Mott-Schottky plots of the control and MSN-SH Sn–Pb PSCs. The curves on top of the data were extracted by linear fitting the drop region of Mott–Schottky plots, and V_{bi} was obtained via the intercept of the straight line with the χ axis.

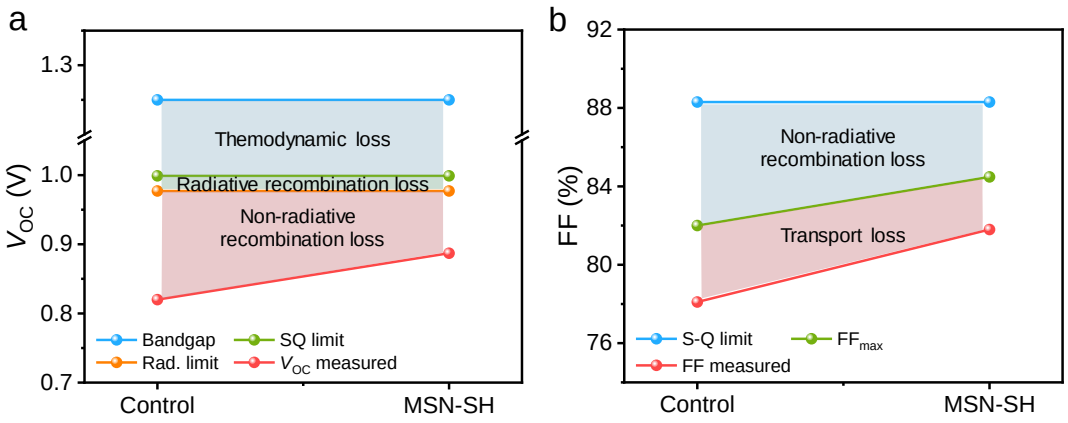

Supplementary Fig. 29. Detailed (**a**) V_{OC} loss analysis and (**b**) FF loss analysis of the control and MSN-SH devices.

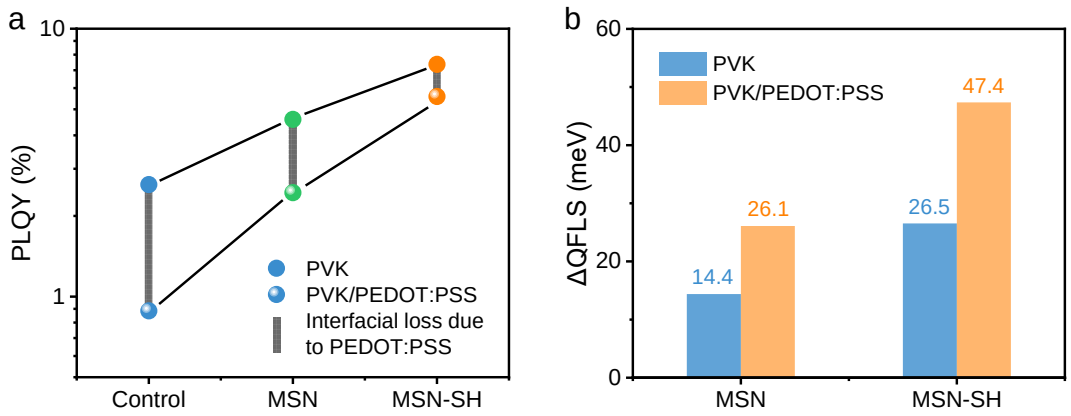

Supplementary Fig. 30. (**a**) PLQY and (**b**) ΔQFLS results for neat perovskite film, PEDOT:PSS/perovskite stacks without and with MSN or MSN-SH treatments. PVK denotes perovskite. Each PLQY value was provided by the average measurement value of five samples in one batch.

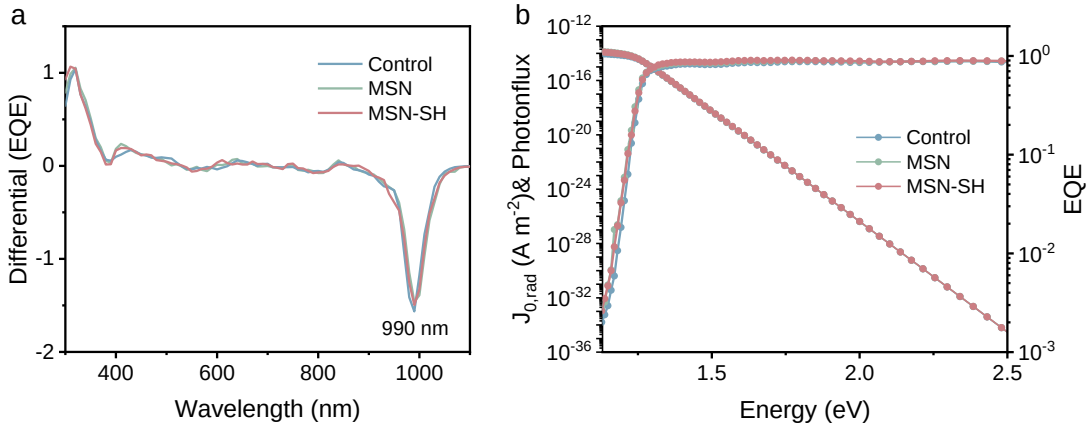

Supplementary Fig. 31. (**a**) d(EQE)/dλ versus wavelength suggests a bandgap of 1.25 eV. (**b**) EQE of the Sn–Pb PSCs. The emitted spectral photon flux calculated when the device is in equilibrium with the black-body (BB) radiation of the environment at 300 K. The $J_{0,rad}$ was calculated to 1.2×10^{-15} mA cm^{-2}.

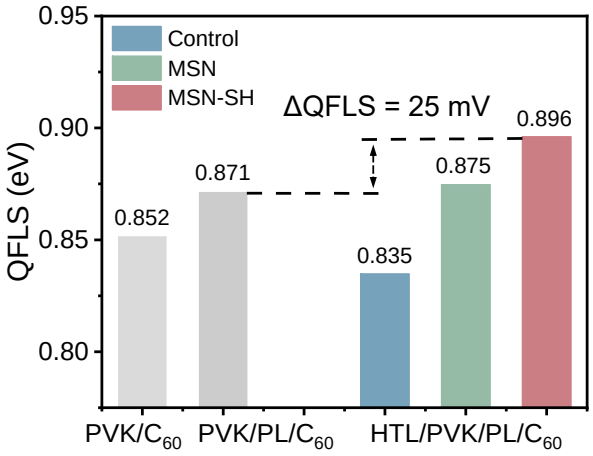

Supplementary Fig. 32. QFLS values for Sn–Pb perovskite films deposited on glass and different substrates with or without passivation layer (PL) and C_{60} coated. The graph shows that the V_{OC} of Sn–Pb PSCs was limited by both PEDOT:PSS and C_{60} layers. The p-interface was almost lossless in the MSN and MSN-SH devices, where PEDOT:PSS layer is causing some additional losses that are being minimized. Meanwhile, we noticed that the QFLS of PEDOT:PSS/MSN-SH/perovskite/$EDAI_2$/C_{60} stacks was 25 mV higher than that of perovskite/$EDAI_2$/C_{60}, which may be related to the improvement of perovskite morphology and quality of the film surface as grown on MSN-SH-coated HTL to reduce C_{60}-induced recombination losses.

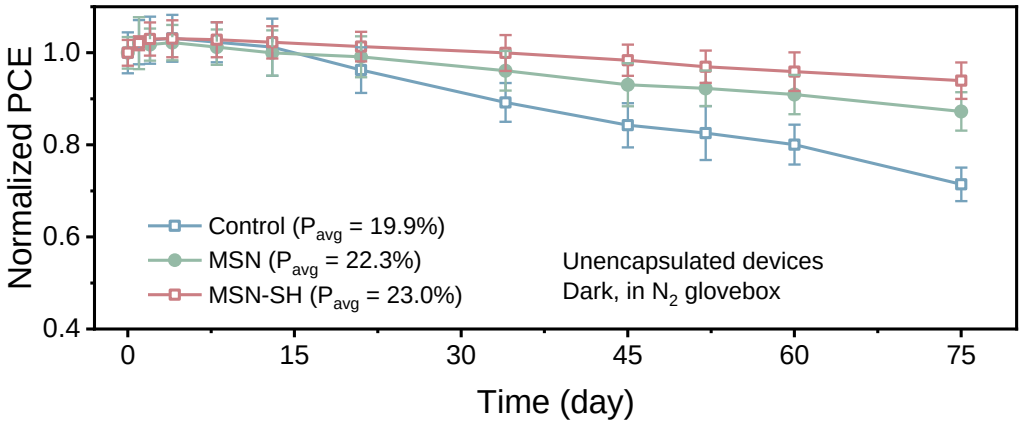

Supplementary Fig. 33. Long-term storage stability of unencapsulated control, MSN, and MSN-SH Sn–Pb PSCs at room temperature under the dark in the N_2 glovebox. P_{avg} denotes the initial average PCE of five devices in one batch. Error bars show the lower and upper PCEs of devices at each condition.

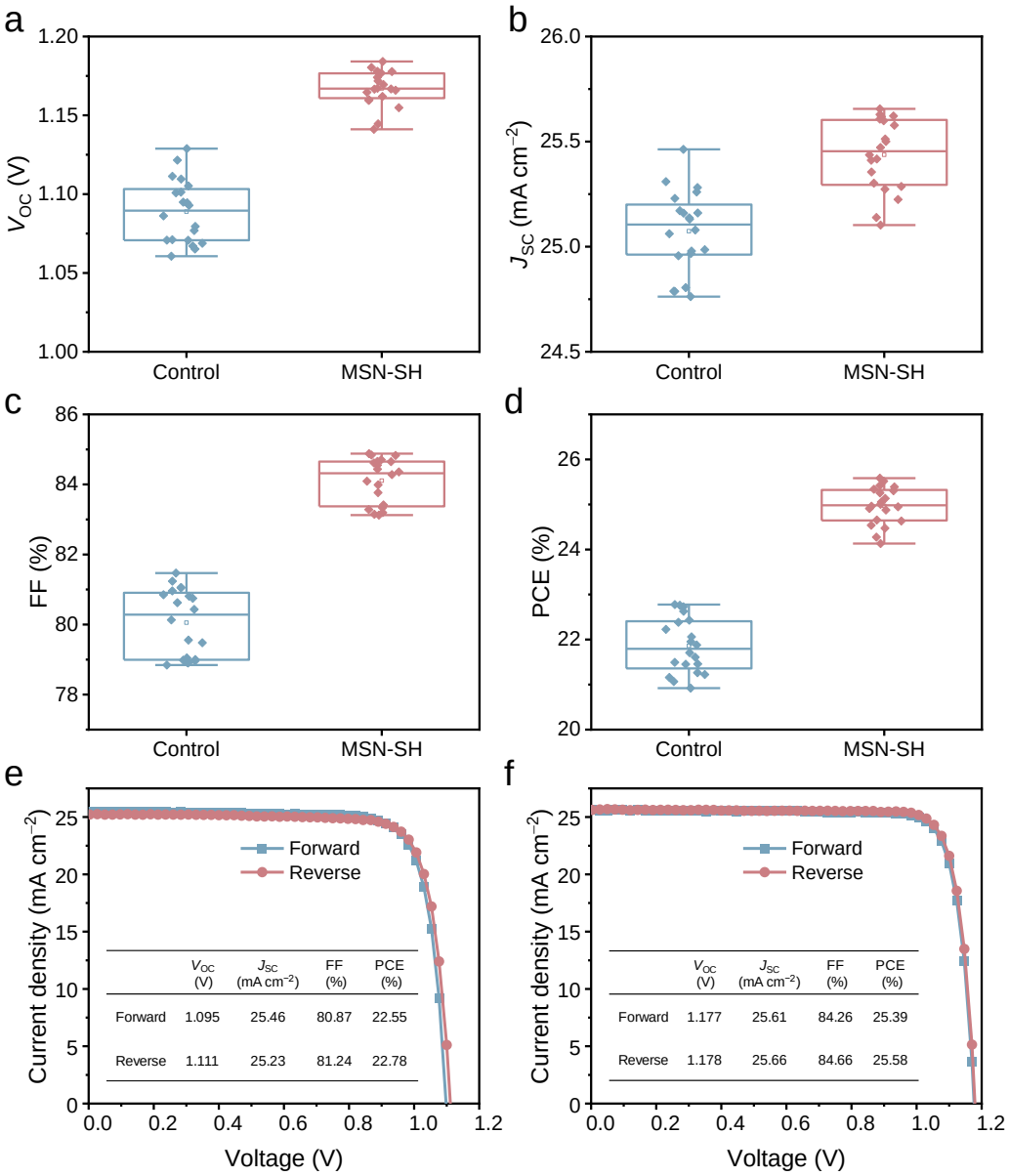

Supplementary Fig. 34. Statistical distribution of the photovoltaic parameters for control and MSN-SH 1.52 eV PSCs. (**a**) V_{OC}, (**b**) J_{SC}, (**c**) FF, and (**d**) PCE values were obtained from the *J*–*V* characteristics of 20 devices. *J*–*V* curves of the champion (**e**) control and (**f**) MSN-SH device under reverse and forward scans.

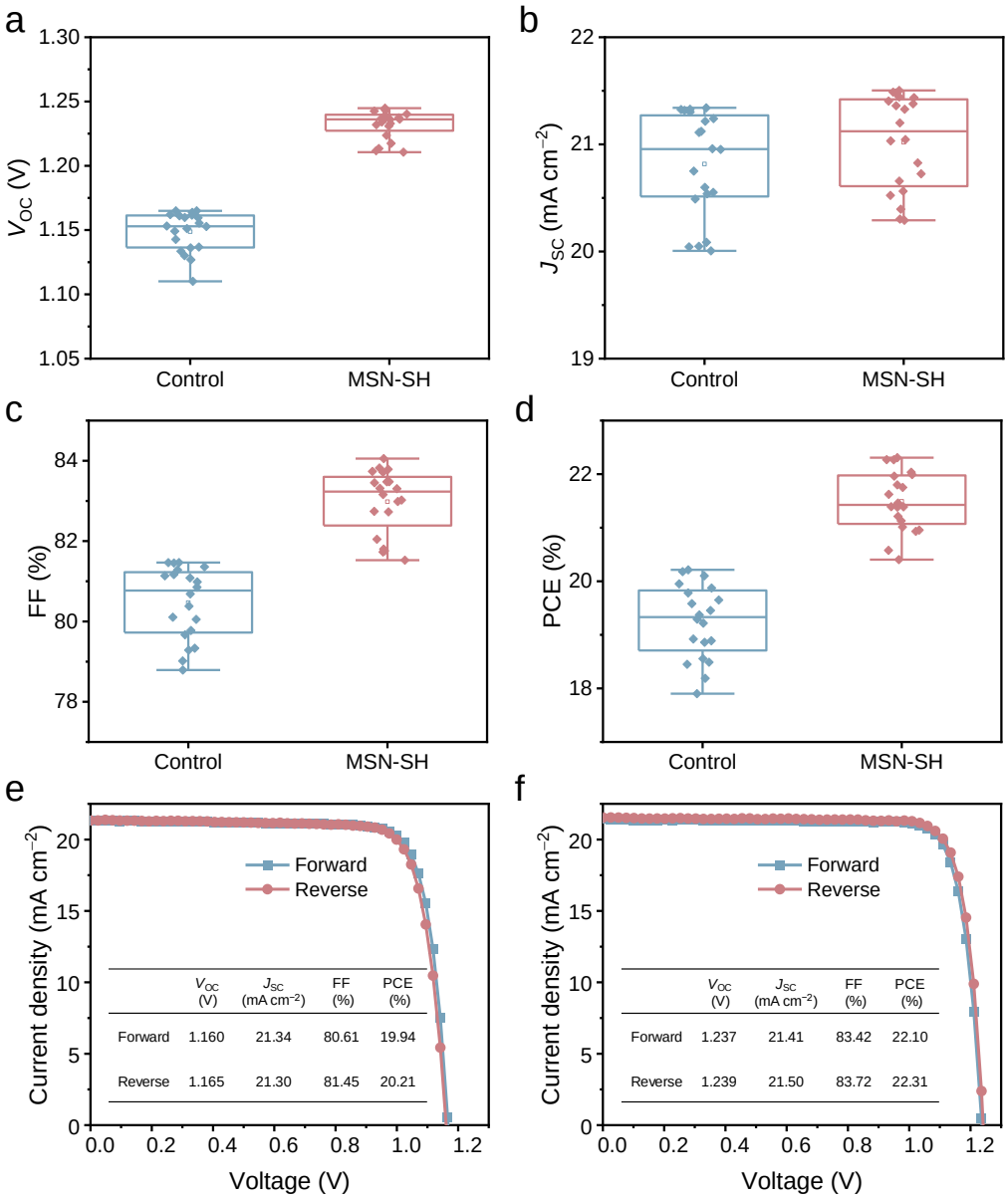

Supplementary Fig. 35. Statistical distribution of the photovoltaic parameters for control and MSN-SH 1.68 eV PSCs. (**a**) V_{OC}, (**b**) J_{SC}, (**c**) FF, and (**d**) PCE values were obtained from the *J*–*V* characteristics of 20 devices. *J*–*V* curves of the champion (**e**) control and (**f**) MSN-SH device under reverse and forward scans.

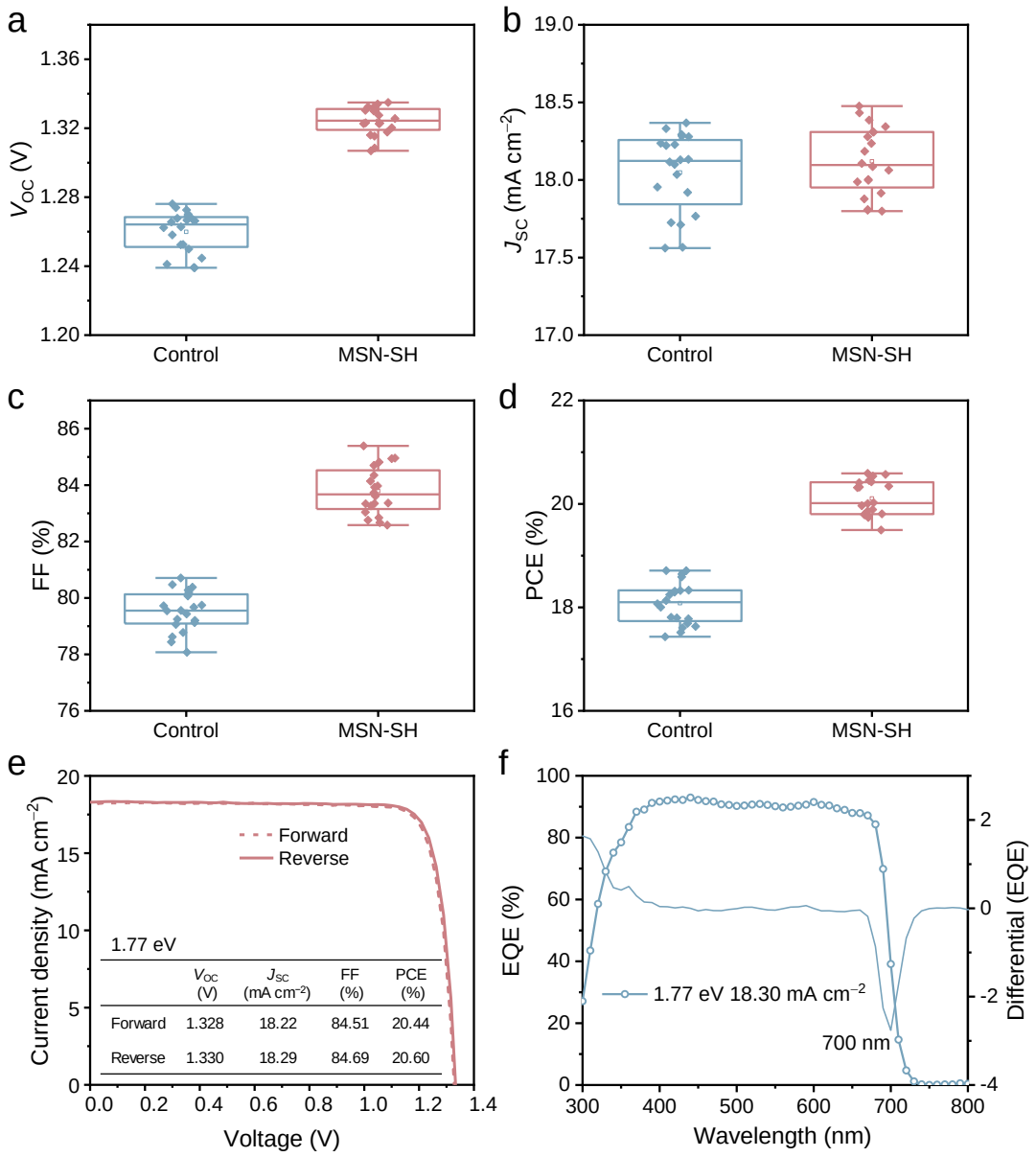

	V_{OC} (V)	J_{SC} (mA cm^{-2})	FF (%)	PCE (%)
Forward	1.328	18.22	84.51	20.44
Reverse	1.330	18.29	84.69	20.60

Supplementary Fig. 36. Statistical distribution of the photovoltaic parameters for control and MSN-SH 1.77 eV WBG PSCs. (**a**) V_{OC}, (**b**) J_{SC}, (**c**) FF, and (**d**) PCE values were obtained from the *J*–*V* characteristics of 20 devices. (**e**) *J*–*V* curves of the champion MSN-SH device under reverse and forward scans. (**f**) EQE spectra of champion MSN-SH device. The d(EQE)/dλ versus wavelength suggests a bandgap of 1.77 eV.

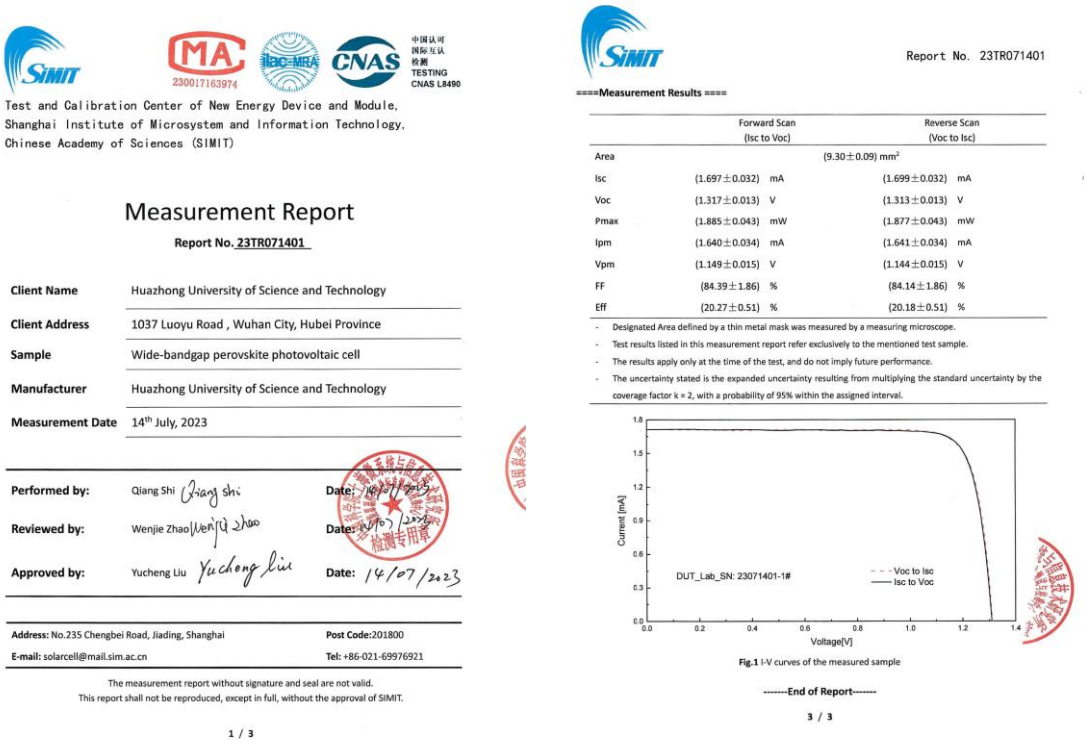

Test and Calibration Center of New Energy Device and Module,
Shanghai Institute of Microsystem and Information Technology,
Chinese Academy of Sciences (SIMIT)

230017163974

TESTING
CNAS L8490

Measurement Report

Report No. 23TR071401

Client Name	Huazhong University of Science and Technology
Client Address	1037 Luoyu Road , Wuhan City, Hubei Province
Sample	Wide-bandgap perovskite photovoltaic cell
Manufacturer	Huazhong University of Science and Technology
Measurement Date	14th July, 2023

Performed by:	Qiang Shi	**Date:** 14/07/2023
Reviewed by:	Wenjie Zhao	**Date:** 14/07/2023
Approved by:	Yucheng Liu	**Date:** 14/07/2023

Address: No.235 Chengbei Road, Jiading, Shanghai **Post Code:**201800
E-mail: solarcell@mail.sim.ac.cn **Tel:** +86-021-69976921

The measurement report without signature and seal are not valid.
This report shall not be reproduced, except in full, without the approval of SIMIT.

1 / 3

Report No. 23TR071401

====Measurement Results ====

	Forward Scan (Isc to Voc)	Reverse Scan (Voc to Isc)
Area	(9.30±0.09) mm²	
Isc	(1.697±0.032) mA	(1.699±0.032) mA
Voc	(1.317±0.013) V	(1.313±0.013) V
Pmax	(1.885±0.043) mW	(1.877±0.043) mW
Ipm	(1.640±0.034) mA	(1.641±0.034) mA
Vpm	(1.149±0.015) V	(1.144±0.015) V
FF	(84.39±1.86) %	(84.14±1.86) %
Eff	(20.27±0.51) %	(20.18±0.51) %

- Designated Area defined by a thin metal mask was measured by a measuring microscope.
- Test results listed in this measurement report refer exclusively to the mentioned test sample.
- The results apply only at the time of the test, and do not imply future performance.
- The uncertainty stated is the expanded uncertainty resulting from multiplying the standard uncertainty by the coverage factor k = 2, with a probability of 95% within the assigned interval.

Fig.1 I-V curves of the measured sample

--------End of Report--------

3 / 3

Supplementary Fig. 37. Certified performance of 1.77 eV WBG PSCs with an aperture area of 0.093 cm^2 based on MSN-SH. The certified PCE is 20.27% with a V_{OC} value of 1.317 V.

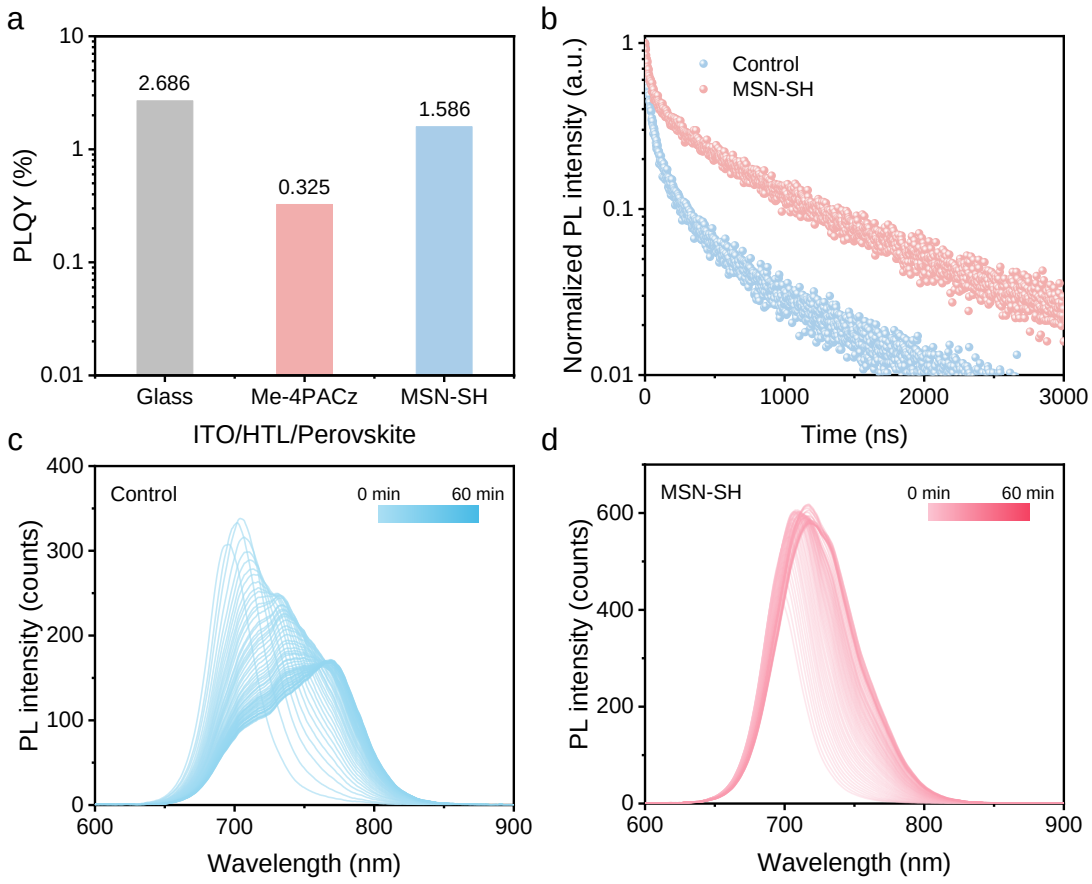

Supplementary Fig. 38. (**a**) PLQY values of WBG perovskite deposited on glass, ITO/Me-4PACz, ITO/Me-4PACz/MSN-SH substrate, respectively. (**b**) TRPL decays were performed on the exposed buried interface of WBG perovskite film deposited on ITO/Me-4PACz (control) and ITO/Me-4PACz/MSN-SH (the MSN-SH sample) substrates. PL spectra of (**c**) control and (**d**) MSN-SH WBG perovskite films under 1 sun illumination for 60 minutes.

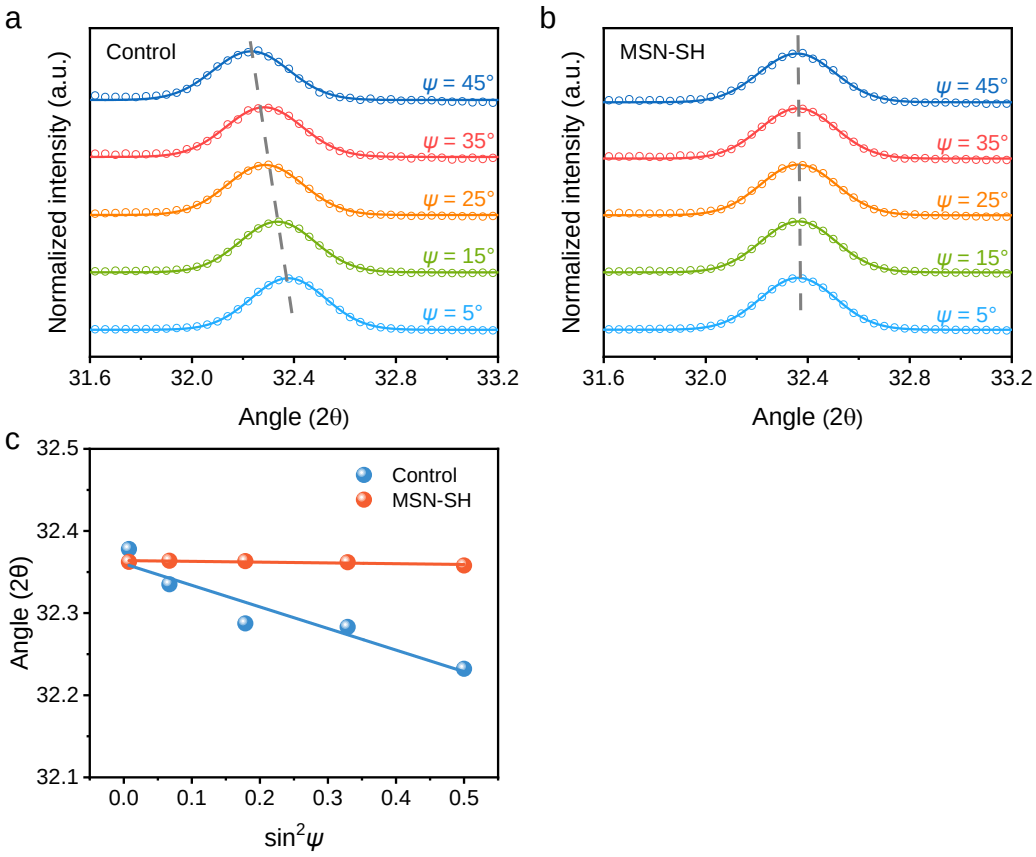

Supplementary Fig. 39. GIXRD patterns performed on the exposed buried interface of (**a**) control and (**b**) MSN-SH WBG perovskite film at different tilt angles from 5 to 45° with an incidence angle of 0.3°. (**c**) Residual strain analysis by linear fitting of 2θ-$\sin^2\phi$ for control and MSN-SH WBG perovskite films. The insertion of MSN-SH material effectively released the tensile stress from 63.3 to 2.3 MPa.

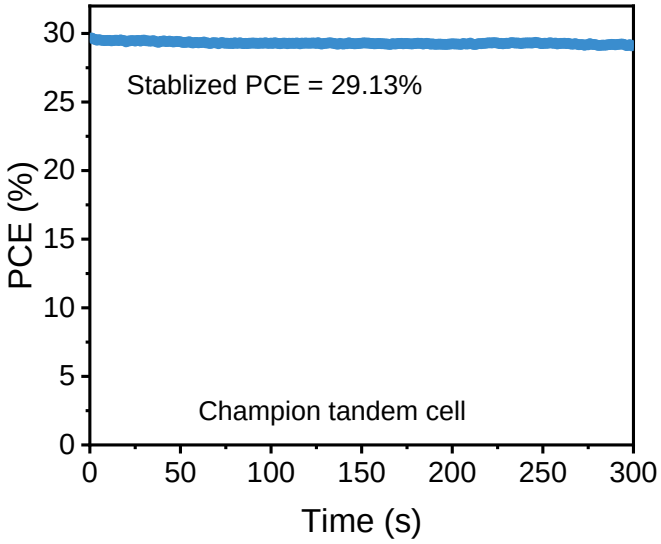

Supplementary Fig. 40. Stabilized power output of the champion MSN-SH tandem device measured by fixing the voltage at 1.87 V under AM1.5G illumination.

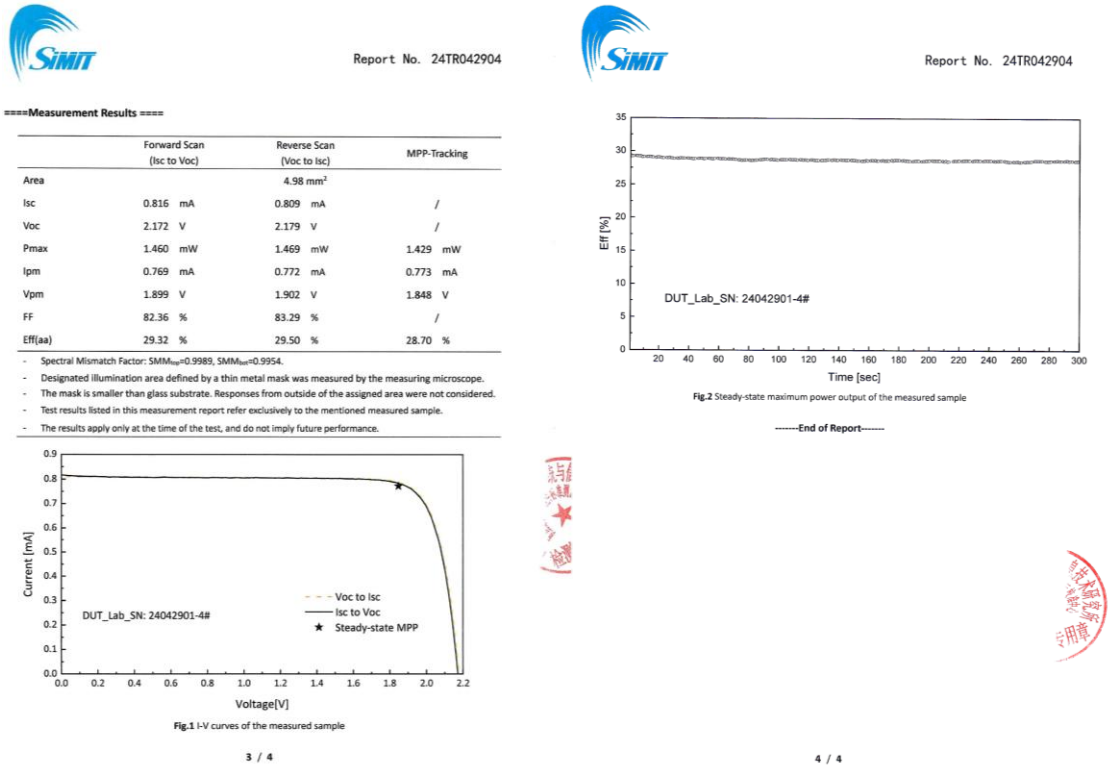

Report No. 24TR042904

====Measurement Results ====

	Forward Scan (Isc to Voc)	Reverse Scan (Voc to Isc)	MPP-Tracking
Area		4.98 mm²	
Isc	0.816 mA	0.809 mA	/
Voc	2.172 V	2.179 V	/
Pmax	1.460 mW	1.469 mW	1.429 mW
Ipm	0.769 mA	0.772 mA	0.773 mA
Vpm	1.899 V	1.902 V	1.848 V
FF	82.36 %	83.29 %	/
Eff(aa)	29.32 %	29.50 %	28.70 %

- Spectral Mismatch Factor: SMM_{fos}=0.9989, SMM_{bot}=0.9954.
- Designated illumination area defined by a thin metal mask was measured by the measuring microscope.
- The mask is smaller than glass substrate. Responses from outside of the assigned area were not considered.
- Test results listed in this measurement report refer exclusively to the mentioned measured sample.
- The results apply only at the time of the test, and do not imply future performance.

Fig.1 I-V curves of the measured sample

3 / 4

Report No. 24TR042904

Fig.2 Steady-state maximum power output of the measured sample

-------End of Report-------

4 / 4

Supplementary Fig. 41. Certified performance of tandem device with an aperture area of 0.0498 cm^2 based on MSN-SH. The certified PCE is 29.50% with an FF value of 83.29% from the scanned *J–V* curve, and a certified steady-state efficiency of 28.70% at a maximum power point of 1.848 V.

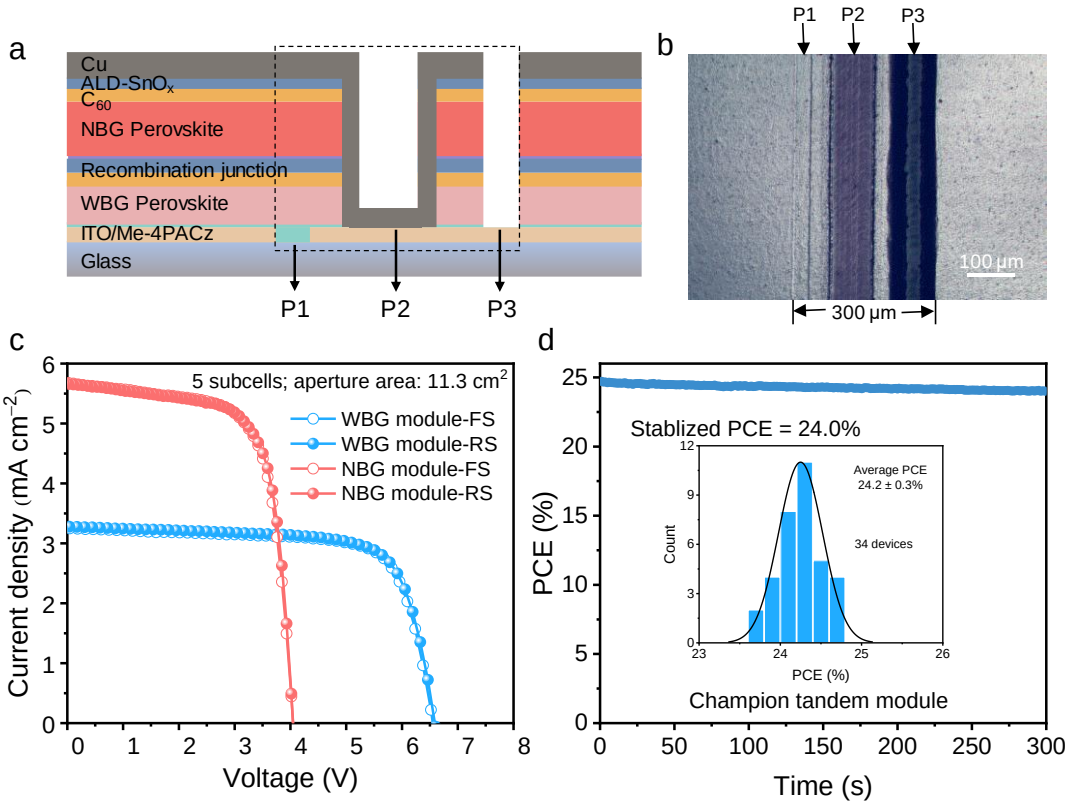

Supplementary Fig. 42. (**a**) Schematic diagram of the fabricated all-perovskite tandem mini-module. (**b**) Optical photo of scribing for subcell separation in tandem mini-modules. (**c**) *J*–*V* curves of the champion WBG and NBG perovskite mini-module under reverse and forward scans. (**d**) Stabilized power output of champion MSN-SH tandem mini-module during a course of 300 s under simulated AM1.5G illumination. (Inset) The PCE distribution of 34 tandem mini-modules, showed an average PCE of 24.2 ± 0.3%.

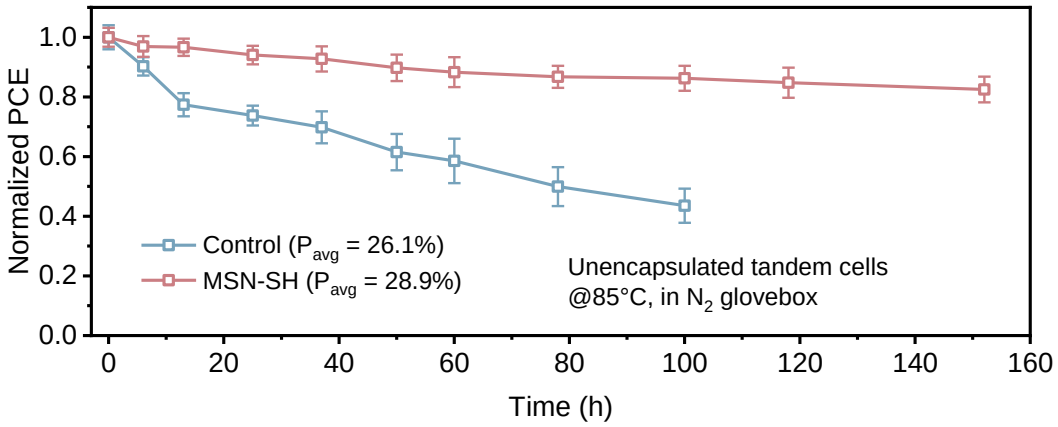

Supplementary Fig. 43. Performance evolution of unencapsulated tandem devices aging at 85°C under the dark in the N_2 glovebox. P_{avg} denotes the initial average PCE of five devices in one batch. Error bars show the lower and upper PCEs of devices at each condition.

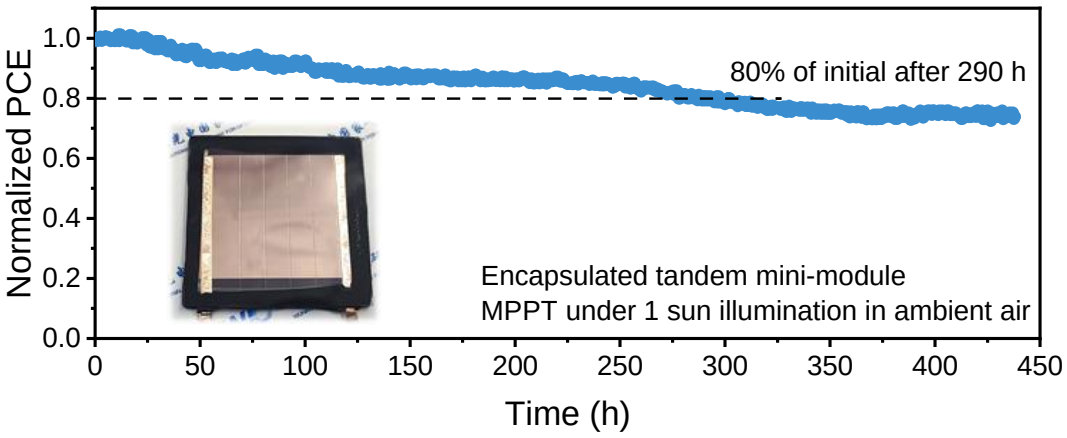

Supplementary Fig. 44. Continuous maximum power point tracking (MPPT) for the encapsulated tandem mini-module under simulated AM1.5G illumination in ambient air. Inset: photograph of the encapsulated tandem mini-module.

Supplementary Table 1. The $Sn^{4+}/(Sn^{4+} + Sn^{2+})$ ratio and binding energy of the Sn^{4+} and Sn^{2+} peaks, as determined from the deconvolution of the $3d_{3/2}$ and $3d_{5/2}$ XPS peak manifolds shown in Fig. 2e-f.

Sample	$Sn^{4+}/$ $(Sn^{4+} + Sn^{2+})$	$3d_{3/2}$ (eV)		$3d_{5/2}$ (eV)	
		Sn^{2+}	Sn^{4+}	Sn^{2+}	Sn^{4+}
Control (fresh)	21.8%	486.53	487.23	494.93	495.63
MSN-SH (fresh)	12.6%	486.41	487.11	494.82	495.52
Control (aged)	52.6%	486.77	487.47	495.26	495.96
MSN-SH (aged)	23.8%	486.71	487.41	495.13	495.83

Supplementary Table 2. Summary of photovoltaic parameters of control, MSN, and MSN-SH NBG PSCs. Average performance parameters of 30 devices for each type are presented.

Devices	V_{OC} (V)	J_{SC} (mA cm^{-2})	FF (%)	PCE (%)
Control NBG	0.802 ± 0.012	31.59 ± 0.51	77.48 ± 0.87	19.64 ± 0.43
(champion device)	(0.820)	(32.01)	(78.15)	(20.53)
MSN NBG	0.851 ± 0.011	32.22 ± 0.36	80.69 ± 0.58	22.13 ± 0.40
(champion device)	(0.860)	(32.58)	(81.28)	(22.77)
MSN-SH NBG	0.877 ± 0.010	32.39 ± 0.29	81.37 ± 0.60	23.10 ± 0.39
(champion device)	(0.887)	(32.77)	(81.67)	(23.74)

Supplementary Table 3. Summary of calculated V_{OC} loss in control and MSN-SH NBG PSCs. Based on the detailed balance theory, the voltage loss in solar cells can be attributed to the three factors.

Samples	E_g (eV)	V_{OC}^{SQ} (V)	V_{OC} (V)	ΔV_1 (mV)	ΔV_2 (mV)	ΔV_3 (mV)
Control	1.25	0.999	0.820	251	21	160
MSN-SH	1.25	0.999	0.887	251	21	94

Supplementary Table 4. PLQY and QFLS values of neat perovskite, HTL/perovskite, and HTL/perovskite/$EDAI_2$/ETL stack.

Sample stacks	PLQY (%)	QFLS (eV)
Glass/PVK	2.619	0.884
Glass/MSN/PVK	4.586	0.898
Glass/MSN-SH/PVK	7.361	0.911
Glass/ITO/PEDOT:PSS/PVK	0.885	0.856
Glass/ITO/PEDOT:PSS/MSN/PVK	2.443	0.882
Glass/ITO/PEDOT:PSS/MSN-SH/PVK	5.586	0.903
Glass/PVK/C_{60}	0.753	0.852
Glass/PVK/$EDAI_2$/C_{60}	1.620	0.871
Glass/ITO/PEDOT:PSS/PVK/$EDAI_2$/C_{60}	0.393	0.835
Glass/ITO/PEDOT:PSS/MSN/PVK/$EDAI_2$/C_{60}	1.835	0.875
Glass/ITO/PEDOT:PSS/MSN-SH/PVK/$EDAI_2$/C_{60}	4.201	0.896

Supplementary Table 5. Summary of photovoltaic parameters of control and MSN-SH WBG PSCs. Average performance parameters of 20 devices for each type are presented.

Devices	V_{OC} (V)	J_{SC} (mA cm^{-2})	FF (%)	PCE (%)
Control WBG	1.260 ± 0.012	18.05 ± 0.26	79.52 ± 0.71	18.08 ± 0.41
(champion device)	(1.276)	(18.22)	(80.47)	(18.71)
MSN-SH WBG	1.324 ± 0.008	18.12 ± 0.22	83.79 ± 0.85	20.11 ± 0.34
(champion device)	(1.330)	(18.29)	(84.69)	(20.60)

Supplementary Table 6. Summary of photovoltaic parameters of control and MSN-SH tandem devices. Average performance parameters of 30 devices for each type are presented.

Devices	V_{OC} (V)	J_{SC} (mA cm^{-2})	FF (%)	PCE (%)
Control tandem	2.042 ± 0.017	15.98 ± 0.16	79.34 ± 0.85	25.90 ± 0.42
(champion device)	(2.048)	(16.18)	(80.75)	(26.76)
MSN-SH tandem	2.165 ± 0.010	16.29 ± 0.09	82.66 ± 0.69	29.16 ± 0.31
(champion device)	(2.176)	(16.33)	(83.38)	(29.63)

Supplementary Table 7. Summary of photovoltaic parameters of champion WBG, NBG, and tandem mini-module.

Devices	Scan	V_{OC} (V)	J_{SC} (mA cm^{-2})	FF (%)	PCE (%)
WBG module	Forward	6.545	3.251	73.95	15.74
	Reverse	6.589	3.279	73.39	15.86
NBG module	Forward	4.046	5.677	69.57	15.98
	Reverse	4.042	5.667	70.25	16.09
Tandem module	Forward	10.38	2.949	80.38	24.61
	Reverse	10.38	2.967	80.32	24.74

Supplementary References

1. Peng, W. et al. Reducing nonradiative recombination in perovskite solar cells with a porous insulator contact. *Science* **379**, 683-690 (2023).
2. Kankala, R. K. et al. Nanoarchitectured structure and surface biofunctionality of mesoporous silica nanoparticles. *Adv. Mater.* **32**, 1907035 (2020).
3. Zhang, X., Zhao, Y., Xie, S. & Sun, L. Fabrication of functionalized porous silica nanoparticles and their controlled release behavior. *J. Drug Delivery Sci. Technol.* **37**, 38-45 (2017).
4. Purikova, O. et al. Free-Blockage Mesoporous Silica Nanoparticles Loaded with Cerium Oxide as ROS-Responsive and ROS-Scavenging Nanomedicine. *Adv. Funct. Mater.* **32**, 2208316 (2022).
5. Pérez-Quintanilla, D., del Hierro, I., Fajardo, M. & Sierra, I. Preparation of 2-mercaptobenzothiazole-derivatized mesoporous silica and removal of Hg(II) from aqueous solution. *J. Environ. Monit.* **8**, 214-222 (2006).
6. Bae, J. A. et al. Effect of pore structure of amine-functionalized mesoporous silica-supported rhodium catalysts on 1-octene hydroformylation. *Microporous Mesoporous Mater.* **123**, 289-297 (2009).
7. Song, S.-W., Hidajat, K. & Kawi, S. Functionalized SBA-15 Materials as Carriers for Controlled Drug Delivery: Influence of Surface Properties on Matrix−Drug Interactions. *Langmuir* **21**, 9568-9575 (2005).
8. Zhang, Y. et al. Spherical mesoporous silica nanoparticles for loading and release of the poorly water-soluble drug telmisartan. *J. Controlled Release* **145**, 257-263 (2010).
9. Lee, J.-W., Lee, D.-K., Jeong, D.-N. & Park, N.-G. Control of crystal growth toward scalable fabrication of perovskite solar cells. *Adv. Funct. Mater.* **29**, 1807047 (2019).
10. Liu, C., Cheng, Y.-B. & Ge, Z. Understanding of perovskite crystal growth and film formation in scalable deposition processes. *Chem. Soc. Rev.* **49**, 1653-1687 (2020).
11. Zhu, C. et al. Strain engineering in perovskite solar cells and its impacts on carrier dynamics. *Nat. Commun.* **10**, 815 (2019).

12. Chen, R. et al. Reduction of bulk and surface defects in inverted methylammonium- and bromide-free formamidinium perovskite solar cells. *Nat. Energy* **8**, 839-849 (2023).
13. Yu, D. et al. Electron-withdrawing organic ligand for high-efficiency all-perovskite tandem solar cells. *Nat. Energy* **9**, 298-307 (2024).
14. Stolterfoht, M. et al. Visualization and suppression of interfacial recombination for high-efficiency large-area pin perovskite solar cells. *Nat. Energy* **3**, 847-854 (2018).
15. Leng, X. et al. Mechanical strengthening of a perovskite-substrate heterointerface for highly stable solar cells. *Energy Environ. Sci.* **17**, 4295-4303 (2024).